

NOTICE: this is the author's version of a work that was accepted for publication in *Computers & Geosciences*. Changes resulting from the publishing process, such as peer review, editing, corrections, structural formatting, and other quality control mechanisms may not be reflected in this document. Changes may have been made to this work since it was submitted for publication. A definitive version was subsequently published in *Computers & Geosciences*, Vol. 54 (2013). DOI: [10.1016/j.cageo.2013.01.014](https://doi.org/10.1016/j.cageo.2013.01.014)

Ps-LAMBDA: Ambiguity Success Rate Evaluation Software for Interferometric Applications

Sandra Verhagen^{a,*}, Bofeng Li^b, Peter J.G. Teunissen^{b,a}

^a*Mathematical Geodesy and Positioning, Delft University of Technology*

^b*GNSS Research Centre, Department of Spatial Sciences, Curtin University*

Abstract

Integer ambiguity resolution is the process of estimating the unknown ambiguities of carrier-phase observables as integers. It applies to a wide range of interferometric applications of which Global Navigation Satellite System (GNSS) precise positioning is a prominent example. GNSS precise positioning can be accomplished anytime and anywhere on Earth, provided that the integer ambiguities of the very precise carrier-phase observables are successfully resolved. As wrongly resolved ambiguities may result in unacceptably large position errors, it is crucial that one is able to evaluate the probability of correct integer ambiguity estimation. This ambiguity success rate depends on the underlying mathematical model as well as on the integer estimation method used. In this contribution, we present the Matlab toolbox Ps-LAMBDA for the evaluation of the ambiguity success rates. It allows users to evaluate all available success rate bounds and approximations for different integer estimators. An assessment of the sharpness of the bounds and approximations is given as well. Furthermore, it is shown how the toolbox

*Tel: +31 15 2784545/Fax: +31 15 2783711

Email address: A.A.Verhagen@TUDelft.nl (Sandra Verhagen)

can be used to assess the integer ambiguity resolution performance for design and research purposes, so as to study for instance the impact of using different GNSS systems and/or different measurement scenarios.

Keywords: Ambiguity Success Rate, GNSS, Interferometry, Integer Estimation, Ps-LAMBDA

1. Introduction

The range of applications depending on precise positioning in real-time with a Global Navigation Satellite System (GNSS) has been growing dramatically in the past decades, and will continue to do so with the advent of more signals and systems by means of modernized GPS, the European Galileo and the Chinese Compass. The applications range from navigation and geodetic surveying to Earth observation, construction, and safety-of-life navigation.

All these applications have in common that they rely on the very precise GNSS carrier-phase observations for precise (and real-time) positioning. These observations are ambiguous by an unknown integer number of cycles. Only if the ambiguities can be resolved correctly, is it possible to obtain accuracies at centimeter-level or below. It is therefore important to assess the probability of correct integer estimation, called the success rate. Although a variety of success rate bounds have been developed, no standard software exists to evaluate these bounds for different integer estimation methods. In this contribution, we introduce the new Matlab tool Ps-LAMBDA for the evaluation of interferometric ambiguity success rates.

Here we briefly address some specific examples of the broad-ranging geoscience applications for which correct integer ambiguity estimation is crucial. For these applications, the success rate tool is valuable, not only for deciding

20 on whether or not to fix the ambiguities in (real-time) data processing algorithms,
21 but also for design and research purposes, so as to study for instance, the impact
22 or potential of using different GNSS systems, different measurement scenarios
23 and/or choice of signals, receivers or baseline lengths.

24 As a first example, we mention the GNSS Real-Time Kinematic (RTK) tech-
25 nique, (Odijk, 2002; Li and Teunissen, 2011; Euler et al., 2004; Takac and Zelzer,
26 2008). It is widely used for mapping, geodetic surveying and network applica-
27 tions, (Blewitt, 1989; Bock, 1996; Strang and Borre, 1997; Leick, 2004; Hofmann-
28 Wellenhof et al., 2008; Teunissen and Kleusberg, 1998). With GNSS-RTK, centimeter-
29 level positioning in real-time can be achieved based on relative positioning to one
30 or more base stations. Cancellation or mitigation of common error sources allows
31 for improved precision, but centimeter-level accuracies can only be achieved after
32 the successful estimation of the integer ambiguities.

33 Recently, the RTK-technique has been extended to the concept of Precise Point
34 Positioning (PPP), (Heroux and Kouba, 1995; Zumberge et al., 1997). With PPP,
35 satellite orbit and clock corrections from a global network of receivers are used to
36 enable subdecimeter accuracies. This has the advantage that PPP does not rely on
37 a dense network of receivers, and thus can be used anywhere on Earth. The newly
38 developed PPP-RTK technique allows to exploit the precise GNSS carrier-phase
39 measurements, such that higher precisions and shorter convergence times become
40 feasible, (Odijk et al., 2012; Geng et al., 2012; Collins et al., 2009; Laurichesse
41 et al., 2009). Hence, also for PPR-RTK, reliable integer estimation is crucial.

42 Another example is GNSS-based georeferencing as used in many remote sens-
43 ing applications. The remote sensing platforms range from survey ships, to air-
44 borne and Unmanned Airborne Vehicles (Everaerts, 2008; Rieke et al., 2011),

45 and even spaceborne platforms, (Buist et al., 2010; Kroes et al., 2005; Leung and
46 Montenbruck, 2005; Huber et al., 2010; Nadarajah et al., 2012). GNSS allows for
47 precise positioning and attitude determination of the platforms, in real-time or in
48 post-processing mode. In either case, to enable precise georeferencing, successful
49 carrier-phase ambiguity resolution is needed.

50 Integer ambiguity resolution is also important in the quality control of GNSS
51 data. Loss-of-lock and/or high receiver dynamics may cause integer cycle slips
52 in the carrier phase data. Successful cycle slip detection and repair is therefore
53 important to maintain the integrity of the data (deLacy et al., 2011; Dai et al.,
54 2009; Wu et al., 2010).

55 Also several non-positioning applications of GNSS can be given as examples.
56 For instance, the use of GNSS stations at fixed locations for deformation moni-
57 toring and change detection, e.g. in tectonic active regions, near volcanoes and in
58 areas susceptible to deformation, (Dong and Bock, 1989; Fernandes et al., 2004;
59 Michel et al., 2001). Or the use of observed GNSS path delays for atmospheric
60 profiling, integrated water vapor measurement and creating ionosphere maps, (Be-
61 vis et al., 1992; Van der Hoeven et al., 2002; Schon and Brunner, 2008; Todorova
62 et al., 2008; Wickert et al., 2009). In all these applications, the precise carrier-
63 phase observables are needed, but the signal of interest can only be extracted once
64 the unknown integer ambiguities are resolved.

65 Next to GNSS, Ps-LAMBDA also applies to all other interferometric tech-
66 niques for which the integer ambiguity resolution problem plays a role. Interfero-
67 metric Synthetic Aperture Radar (InSAR) is one example. The associated interfer-
68 ometric phase observations can be described by a linear function of topographic
69 height, surface deformation, and the integer ambiguity parameters. Precise esti-

70 mation of the surface deformation is thus dependent on successful resolution of
71 the integer parameters, (Hanssen et al., 2001). Similarly, the fringe phase obser-
72 vations from Very Long Baseline Interferometry (VLBI) include unknown integer
73 ambiguities, which need to be resolved in order to achieve the 1 mm global posi-
74 tioning accuracy, (Hobiger et al., 2009). As another example, we mention the use
75 of acoustic waves for precise positioning, e.g. for indoor and underwater applica-
76 tions, (Das Neves Viegas and Cunha, 2007). Again integer ambiguity resolution
77 is the key.

78

79 As the above examples show, the evaluation of the integer ambiguity success rate
80 is important for a wide range of interferometric applications. In this contribu-
81 tion, we use GNSS and its models to present and describe the Matlab toolbox
82 Ps-LAMBDA. Section 2 presents the basic GNSS model and the essence of cor-
83 rect integer ambiguity estimation. Section 3 reviews the three integer estimators
84 integer rounding (IR), integer bootstrapping (IB) and integer least squares (ILS).
85 In Section 4, the multivariate success rate is defined and the Ps-LAMBDA soft-
86 ware to evaluate the success rate is described . In Section 5 the available success
87 rate bounds and approximations of IR, IB and ILS are presented, together with
88 an assessment of their performance. Section 6 presents an example of how the
89 toolbox can be used to assess the performance potential of the American GPS, the
90 European Galileo, and the Chinese Compass satellite systems.

Table 1: Overview of GNSS frequencies of open signals.

Band	Frequency	GPS	Galileo	Compass
L1	1575.42 MHz	X	X	
B1	1561.098 MHz			X
L2	1227.60 MHz	X		
E5b/B2	1207.14 MHz		X	X
L5/E5a	1176.45 MHz	X	X	

91 2. GNSS model and integer estimation

92 2.1. GNSS observation equations

93 Precise GNSS positioning relies on the carrier-phase observations, which can
 94 be observed with millimeter precision versus decimeter precision for the pseudor-
 95 ange observations. The frequencies of the GPS, Galileo and Compass open signals
 96 are given in Table 1. Glonass is not considered because ambiguity resolution is
 97 generally not applied as Glonass applies Frequency Division Multiple Access.

98 The pseudorange and carrier-phase observables on frequency j and satellite-
 99 receiver pair $s - r$ at epoch t are denoted as $p_{r,j}^s(t)$ and $\phi_{r,j}^s(t)$, respectively. Their
 100 observation equations are formulated as , cf.(Hofmann-Wellenhof et al., 2001;
 101 Teunissen and Kleusberg, 1998; Leick, 2004; Strang and Borre, 1997; Misra and
 102 Enge, 2001):

$$\begin{aligned}
 p_{r,j}^s(t) &= \rho_r^s(t) + T_r^s(t) + \mu_j I_r^s(t) + c dt_{r,j}^s(t) + e_r^s(t) \\
 \phi_{r,j}^s(t) &= \rho_r^s(t) + T_r^s(t) - \mu_j I_r^s(t) + c \delta t_{r,j}^s(t) + \lambda_j M_{r,j}^s + \epsilon_r^s(t)
 \end{aligned}
 \tag{1}$$

104 where ρ_r^s is the satellite-receiver range, T_r^s is the troposphere delay, I_r^s is the iono-
 105 sphere delay, $dt_{r,j}^s$ and $\delta t_{r,j}^s$ are the pseudo-range and carrier-phase satellite-receiver

106 clock biases, $M_{r,j}^s$ is the time-invariant carrier-phase ambiguity, c is the speed
 107 of light, λ_j is the wavelength for frequency j , $\mu_j = (\lambda_j/\lambda_1)^2$, and e_r^s and ϵ_r^s are
 108 the remaining error terms, respectively. The real-valued carrier-phase ambiguity
 109 $M_{r,j}^s = \phi_{r,j}(t_0) + \phi_j^s(t_0) + N_{r,j}^s$ is the sum of the initial satellite-receiver phases and
 110 the integer ambiguity $N_{r,j}^s$.

111 The structure of the observation equations of the pseudorange and carrier-
 112 phase observables is the same, only that the latter contains an ambiguity term.
 113 This implies that if the ambiguities can be resolved, the carrier-phase observations
 114 will start to act as very precise pseudorange observations.

115 The initial phases and clock biases present in Eq.(1) can be eliminated through
 116 differencing the observation equations. The so-called double differenced (DD)
 117 observation equations, using simultaneous observations from two receivers and
 118 two satellites, take the form:

$$\begin{aligned}
 119 \quad p_{qr,j}^{ls}(t) &= \rho_{qr}^{ls}(t) + T_{qr}^{ls}(t) + \mu_j I_{qr}^{ls}(t) + e_{qr}^{ls}(t) \\
 \phi_{qr,j}^{ls}(t) &= \rho_{qr}^{ls}(t) + T_{qr}^{ls}(t) - \mu_j I_{qr}^{ls}(t) + \lambda_j N_{qr,j}^{ls} + \epsilon_{qr}^{ls}(t)
 \end{aligned} \tag{2}$$

120 where $p_{qr,j}^{ls}(t) = (p_{r,j}^s(t) - p_{r,j}^l(t)) - (p_{q,j}^s(t) - p_{q,j}^l(t))$, and similar notation for the
 121 other DD variates. The DD troposphere slant delays are usually reduced to a
 122 single DD zenith delay T_{qr}^{zenith} by means of mapping functions. The DD ionosphere
 123 delays can usually be neglected for baselines shorter than 15 km. For longer
 124 baselines, a priori ionosphere corrections can be used. In that case the uncertainty
 125 of those corrections should be taken into account.

126 Under the assumption that the error terms e_{qr}^{ls} and ϵ_{qr}^{ls} in Eq.(2) are zero-mean
 127 variables, the observation equations can be used to set up a mixed integer linear
 128 model, as some of the parameters are reals and others are integer.

129 The observation equations in Eq.(2) are parameterized in terms of the satellite-

130 receiver ranges $\rho_{qr}^{ls}(t)$, which depend on both the satellite and receiver positions.
 131 Assuming the satellite orbits known, these ranges can be linearized with respect to
 132 the unknown receiver coordinates. The linearized observation equations obtained
 133 in this way are then parameterized in terms of the between-receiver baseline vector
 134 increments, and the model is an example of a mixed integer linearized model.

135 2.2. Solving the GNSS model

136 The mixed integer linear(ized) model can now be defined as:

$$137 \quad \mathbf{y} \sim N(\mathbf{A}\mathbf{a} + \mathbf{B}\mathbf{b}, \mathbf{Q}_{yy}), \quad \mathbf{a} \in \mathbb{Z}^n, \quad \mathbf{b} \in \mathbb{R}^p \quad (3)$$

138 The notation " \sim " is used to describe "distributed as". The m -vector \mathbf{y} contains
 139 the pseudorange and carrier-phase observables, the n -vector \mathbf{a} contains the DD
 140 integer ambiguities, \mathbf{b} is the real-valued parameter vector of length p , including
 141 baseline or position components and possibly tropospheric and ionospheric delay
 142 parameters. The coefficient matrices are $\mathbf{A} \in \mathbb{R}^{m \times n}$ and $\mathbf{B} \in \mathbb{R}^{m \times p}$, with $[\mathbf{A} \ \mathbf{B}]$
 143 of full column rank. The variance-covariance (VC-) matrix \mathbf{Q}_{yy} is an $m \times m$ pos-
 144 itive definite matrix. In most GNSS applications, the underlying distribution is
 145 assumed to be the multivariate normal distribution.

146 In general, a three-step procedure is employed to solve model (3) based on the
 147 least squares criterion. In practice, a user may want to include a validation step
 148 after step 1 and step 2.

149 *Step 1: Float solution*

150 In the first step, the integer property of the ambiguities \mathbf{a} is discarded and the
 151 so-called float solution can be obtained with standard least squares:

$$152 \quad \begin{bmatrix} \hat{\mathbf{a}} \\ \hat{\mathbf{b}} \end{bmatrix} = \left(\begin{bmatrix} \mathbf{A}^T \\ \mathbf{B}^T \end{bmatrix} \mathbf{Q}_{yy}^{-1} \begin{bmatrix} \mathbf{A} & \mathbf{B} \end{bmatrix} \right)^{-1} \begin{bmatrix} \mathbf{A}^T \\ \mathbf{B}^T \end{bmatrix} \mathbf{Q}_{yy}^{-1} \mathbf{y} \quad (4)$$

153 with:

$$154 \begin{bmatrix} \hat{\mathbf{a}} \\ \hat{\mathbf{b}} \end{bmatrix} \sim N \left(\begin{bmatrix} \mathbf{a} \\ \mathbf{b} \end{bmatrix}, \begin{bmatrix} \mathbf{Q}_{\hat{\mathbf{a}}\hat{\mathbf{a}}} & \mathbf{Q}_{\hat{\mathbf{a}}\hat{\mathbf{b}}} \\ \mathbf{Q}_{\hat{\mathbf{b}}\hat{\mathbf{a}}} & \mathbf{Q}_{\hat{\mathbf{b}}\hat{\mathbf{b}}} \end{bmatrix} \right) \quad (5)$$

155 $\mathbf{Q}_{\hat{\mathbf{a}}\hat{\mathbf{a}}}$ and $\mathbf{Q}_{\hat{\mathbf{b}}\hat{\mathbf{b}}}$ are the VC-matrices of the float ambiguity and baseline estimators,
156 respectively.

157 *Step 2: Integer estimation*

158 In the second step, the float ambiguity estimate $\hat{\mathbf{a}}$ is used to compute the cor-
159 responding integer ambiguity estimate, denoted as

$$160 \check{\mathbf{a}} = \mathcal{I}(\hat{\mathbf{a}}) \quad (6)$$

161 with $\mathcal{I} : \mathbb{R}^n \mapsto \mathbb{Z}^n$ the integer mapping from the n -dimensional space of reals
162 to the n -dimensional space of integers. In this step, there are different choices of
163 mapping function \mathcal{I} possible, which correspond to the different integer estimation
164 methods. Popular choices are integer least squares (ILS), integer bootstrapping
165 (IB) and integer rounding (IR). Each of the methods will be discussed in more
166 detail in the following subsections.

167 *Step 3: Fixed solution*

168 In the third step, the float solution of the remaining real-valued parameters
169 solved in the first step are updated using the fixed integer parameters,

$$170 \check{\mathbf{b}} = \hat{\mathbf{b}} - \mathbf{Q}_{\hat{\mathbf{b}}\hat{\mathbf{a}}} \mathbf{Q}_{\hat{\mathbf{a}}\hat{\mathbf{a}}}^{-1} (\hat{\mathbf{a}} - \check{\mathbf{a}}) \quad (7)$$

171 This solution is referred to as the fixed baseline solution.

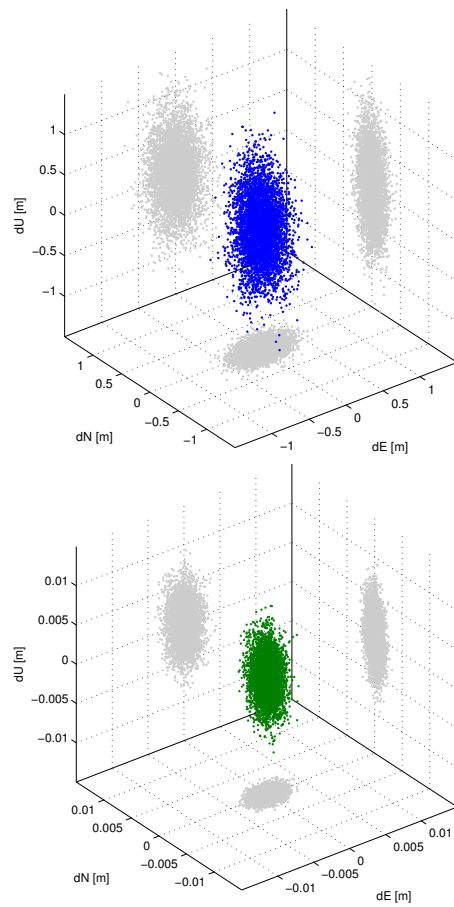


Figure 1: Position errors in East (dE), North (dN) and Up (dU) direction in meters for ambiguity float solutions (top panel), ambiguity fixed solutions (bottom panel). Note the different scales in the top and bottom panels.

172 *2.3. Essence of correct integer estimation*

173 A very high positioning performance can only be guaranteed if the estimated
 174 integer ambiguities are correct. It is therefore very important to assess the proba-
 175 bility of correct integer estimation. This probability is called the success rate and
 176 only if it is very close to 1, it is possible to rely on the integer solution without
 177 further validation. In that case the integer ambiguity solution can be assumed to

178 be deterministic, and the VC-matrix of the fixed baseline solution is obtained by
 179 application of the propagation law of variances to Eq.(7):

$$180 \quad \mathbf{Q}_{\check{b}\check{b}} = \mathbf{Q}_{\hat{b}\hat{b}} - \mathbf{Q}_{\hat{b}\hat{a}}\mathbf{Q}_{\hat{a}\hat{a}}^{-1}\mathbf{Q}_{\hat{a}\hat{b}} \quad (8)$$

181 In general $\mathbf{Q}_{\check{b}\check{b}} \ll \mathbf{Q}_{\hat{b}\hat{b}}$, since after successful ambiguity fixing the carrier-phase
 182 measurements start to act as very precise pseudorange measurements. Figure 1
 183 shows a scatterplot of the float and fixed position errors based on 10,000 solutions
 184 with single epoch, dual-frequency GPS for a short baseline; the success rate is
 185 equal to 1. It can be observed that the precision is improved with a factor 100, in
 186 agreement with the difference in code and carrier-phase measurement noise.

187 However, incorrect integer ambiguity estimation may result in the opposite
 188 effect in terms of positioning accuracy: rather than a dramatic precision improve-
 189 ment, a wrong ambiguity solution can cause very large position errors, exceeding
 190 those of the float solution. This is illustrated in Figure 2, which shows a scatter-
 191 plot of horizontal float position errors for a case where the ambiguities are fixed
 192 correctly in only 93% of the cases. The corresponding fixed solutions are shown
 193 as either red or green dots: red if the ambiguities are fixed incorrectly, green if
 194 they are fixed correctly. It can be seen that in all cases where the ambiguities
 195 were fixed correctly, the position errors are very small. However, in case of un-
 196 successful integer estimation the corresponding position errors tend to be of the
 197 same size or even much larger than the corresponding float position errors. The
 198 figure shows only the horizontal positioning results, for the vertical component
 199 the errors can be as large as 8 meters in this example. This clearly shows that
 200 the fixed solution should only be used if the success rate is very high. Section 4
 201 presents the Ps-LAMBDA toolbox which allows to evaluate the success rate of
 202 integer estimation.

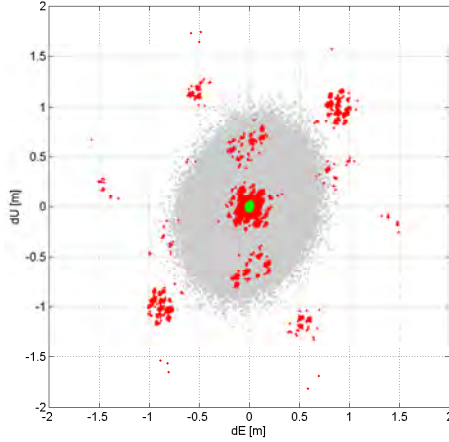


Figure 2: Scatterplot of horizontal position errors in meters for float solution (grey dots) and corresponding fixed solution. In this case, 93% of the solutions were correctly fixed (green dots), and 7% was wrongly fixed (red dots).

203 3. Admissible integer estimation

204 As previously mentioned there are many ways of computing an integer ambi-
 205 guity vector $\check{\mathbf{a}}$ from its real-valued counterpart $\hat{\mathbf{a}}$. To each such method belongs
 206 a different mapping $\mathcal{I} : \mathbb{R}^n \mapsto \mathbb{Z}^n$. Due to the discrete nature of \mathbb{Z}^n , the map \mathcal{I}
 207 will not be one-to-one, but instead a many-to-one map. This implies that different
 208 real-valued ambiguity vectors will be mapped to the same integer vector. One can
 209 therefore assign a subset $\mathcal{P}_z \subset \mathbb{R}^n$ to each integer vector $\mathbf{z} \in \mathbb{Z}^n$:

$$210 \quad \mathcal{P}_z = \{\mathbf{x} \in \mathbb{R}^n \mid \mathbf{z} = \mathcal{I}(\mathbf{x})\}, \quad \mathbf{z} \in \mathbb{Z}^n \quad (9)$$

211 The subset \mathcal{P}_z contains all real-valued ambiguity vectors that will be mapped by
 212 \mathcal{I} to the same integer vector $\mathbf{z} \in \mathbb{Z}^n$. This subset is referred to as the *pull-in region*
 213 of \mathbf{z} . It is the region in which all ambiguity float solutions are pulled to the same
 214 fixed ambiguity vector \mathbf{z} .

215 Using the pull-in regions, one can give an explicit expression for the corre-
 216 sponding integer ambiguity estimator. It reads

$$217 \quad \check{\mathbf{a}} = \sum_{\mathbf{z} \in \mathbb{Z}^n} \mathbf{z} \mathcal{P}_{\mathbf{z}}(\hat{\mathbf{a}}), \quad \mathcal{P}_{\mathbf{z}}(\hat{\mathbf{a}}) = \begin{cases} 1 & \text{if } \hat{\mathbf{a}} \in \mathcal{P}_{\mathbf{z}} \\ 0 & \text{otherwise.} \end{cases} \quad (10)$$

218 Since the pull-in regions define the integer estimator completely, one can define
 219 classes of integer estimators by imposing various conditions on the pull-in regions.
 220 One such class is referred to as the class of admissible integer estimators. This
 221 class was introduced in (Teunissen, 1999b) and it is defined as follows.

222

223 **Definition**

224 The integer estimator $\check{\mathbf{a}} = \sum_{\mathbf{z} \in \mathbb{Z}^n} \mathbf{z} \mathcal{P}_{\mathbf{z}}(\hat{\mathbf{a}})$ is said to be *admissible* if

- (i) $\bigcup_{\mathbf{z} \in \mathbb{Z}^n} \mathcal{P}_{\mathbf{z}} = \mathbb{R}^n$
- 225 (ii) $Int(\mathcal{P}_{\mathbf{z}_1}) \cap Int(\mathcal{P}_{\mathbf{z}_2}) = \emptyset, \quad \forall \mathbf{z}_1, \mathbf{z}_2 \in \mathbb{Z}^n, \mathbf{z}_1 \neq \mathbf{z}_2$
- (iii) $\mathcal{P}_{\mathbf{z}} = \mathbf{z} + \mathcal{P}_{\mathbf{0}}, \quad \forall \mathbf{z} \in \mathbb{Z}^n$

226 This definition is motivated as follows. The first condition states that the pull-in
 227 regions should not leave any gaps and the second that they should not overlap.
 228 The absence of gaps is needed in order to be able to map any float solution $\hat{\mathbf{a}} \in \mathbb{R}^n$
 229 to \mathbb{Z}^n , while the absence of overlaps is needed to guarantee that the float solution
 230 is mapped to just one integer vector. The third and last condition of the definition
 231 follows from the requirement that $I(\mathbf{x} + \mathbf{z}) = I(\mathbf{x}) + \mathbf{z}, \forall \mathbf{x} \in \mathbb{R}^n, \mathbf{z} \in \mathbb{Z}^n$. It states
 232 that when the float solution is perturbed by $\mathbf{z} \in \mathbb{Z}^n$, the corresponding integer
 233 solution is perturbed by the same amount. This property allows one to apply the
 234 *integer remove-restore* technique: $I(\hat{\mathbf{a}} - \mathbf{z}) + \mathbf{z} = I(\hat{\mathbf{a}})$.

235 Integer rounding, integer bootstrapping and integer least squares are all exam-
 236 ples of admissible integer estimation methods.

237 3.1. \mathbf{Z} -transformations

238 It will be explained later that it may be useful to apply a so-called \mathbf{Z} -transformation
 239 to the ambiguity parameters. A matrix is called a \mathbf{Z} -transformation if it is one-to-
 240 one (i.e. invertible) and integer (Teunissen, 1995a). Such transformations leave
 241 the integer nature of the parameters intact. If a certain integer estimator is \mathbf{Z} -
 242 invariant it means that if the float solution is \mathbf{Z} -transformed, the integer solution
 243 transforms accordingly. Hence:

$$244 \quad \check{\mathbf{z}} = \mathbf{Z}^T \check{\mathbf{a}} \quad \text{if} \quad \hat{\mathbf{z}} = \mathbf{Z}^T \hat{\mathbf{a}} \quad (11)$$

245 A very useful \mathbf{Z} -transformation is the decorrelating \mathbf{Z} -transformation, (Teu-
 246 nissen, 1993, 1994, 1995a,b). It results in a more diagonal VC-matrix:

$$247 \quad \mathbf{Q}_{\hat{\mathbf{z}}\hat{\mathbf{z}}} = \mathbf{Z}^T \mathbf{Q}_{\hat{\mathbf{a}}\hat{\mathbf{a}}} \mathbf{Z} \quad (12)$$

248 3.2. Integer rounding

249 The simplest way to obtain an integer vector from the real-valued float solution
 250 is to round each of the entries of $\hat{\mathbf{a}}$ to its nearest integer. The corresponding integer
 251 estimator reads

$$252 \quad \check{\mathbf{a}}_{\text{IR}} = ([\hat{a}_1], \dots, [\hat{a}_n])^T \quad (13)$$

253 where $[\cdot]$ stands for rounding to the nearest integer.

254 The pull-in regions for rounding are n -dimensional unit cubes centred at the
 255 integer grid points:

$$256 \quad \mathcal{P}_{\mathbf{z}, \text{IR}} = \{\mathbf{x} \in \mathbb{R}^n \mid |c_i^T(\mathbf{x} - \mathbf{z})| \leq \frac{1}{2}, i = 1, \dots, n\}, \mathbf{z} \in \mathbb{Z}^n \quad (14)$$

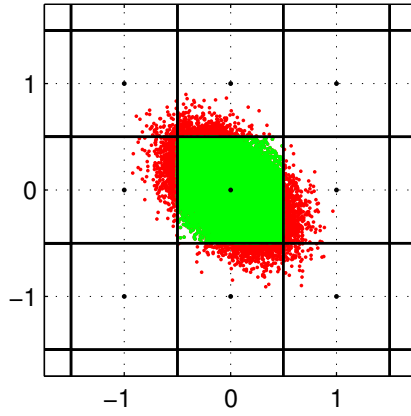
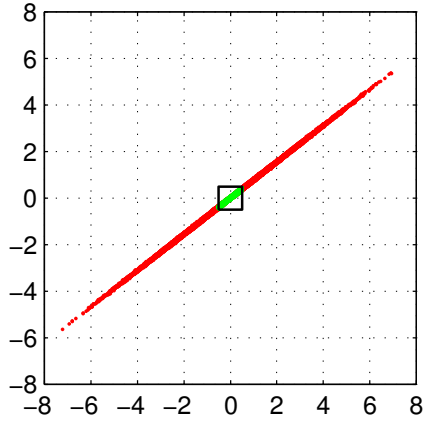


Figure 3: 2D Pull-in regions for integer rounding (IR) and 50,000 float solutions. Top: original ambiguities $\hat{\mathbf{a}}$ [cycles]; Bottom: \mathbf{Z} -decorrelated ambiguities $\hat{\mathbf{z}}$ [cycles].

257 with \mathbf{c}_i the unit vector have a 1 as its i th entry and 0's otherwise.

258 In general, the rounding estimator is not \mathbf{Z} -invariant, i.e. $\check{\mathbf{z}}_{\text{IR}} \neq \mathbf{Z}^T \check{\mathbf{a}}_{\text{IR}}$. Only
 259 if \mathbf{Z} is a permutation matrix, and thus the transformation is a simple reordering
 260 of the ambiguities, the estimator is \mathbf{Z} -invariant. Note that the pull-in regions of
 261 rounding remain unaffected by the \mathbf{Z} -transformation.

262 Figure 3 shows an example for a 2-dimensional (2D) ambiguity vector. 50,000

263 samples of float ambiguities for a given VC-matrix $Q_{\hat{a}\hat{a}}$ were simulated; these are
 264 shown as the red and green dots. The top panel shows the original float samples
 265 (before \mathbf{Z} -decorrelation), and the pull-in region $\mathcal{P}_{0,IR}$, in which all the green sam-
 266 ples reside. Hence, for all those samples the $\mathbf{0}$ -vector is obtained after rounding.
 267 The bottom panel shows the corresponding \mathbf{Z} -decorrelated float ambiguity sam-
 268 ples, as well as the surrounding pull-in regions. In this case, many more float
 269 samples reside in $\mathcal{P}_{0,IR}$: 95% versus 23% before \mathbf{Z} -decorrelation. This shows that
 270 the choice for the parameterization of the float ambiguity vector is very important
 271 in case of integer rounding.

272 3.3. Integer bootstrapping

273 The integer bootstrapping (IB) estimator still makes use of integer rounding,
 274 but it takes some of the correlation between the ambiguities into account. The IB
 275 estimator follows from a sequential least squares adjustment and it is computed as
 276 follows. If n ambiguities are available, one starts with the most precise ambiguity.
 277 Let the n th ambiguity be the most precise one, hence we start with rounding \hat{a}_n
 278 to the nearest integer. The remaining float ambiguities are corrected by virtue of
 279 their correlation with the last ambiguity. Then the last-but-one, but now corrected,
 280 real-valued ambiguity estimate is rounded to its nearest integer and all remaining
 281 $(n - 2)$ ambiguities are then again corrected, but now by virtue of their correlation
 282 with this ambiguity. This process is continued until all ambiguities are considered.

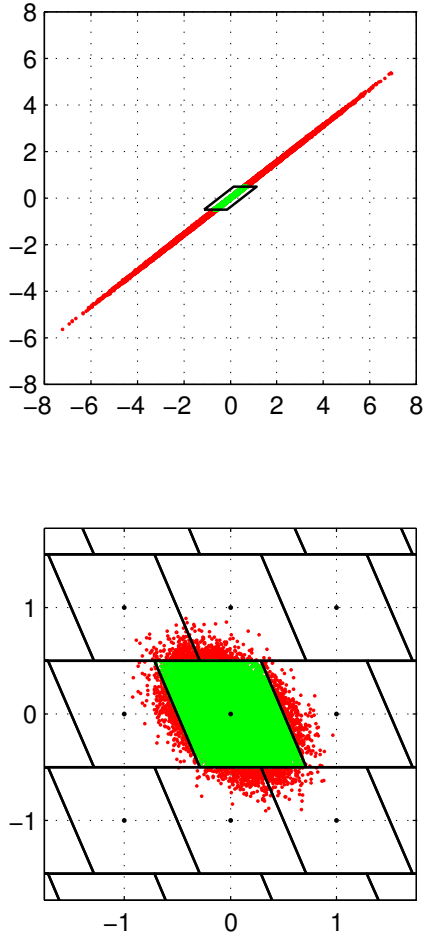


Figure 4: 2D pull-in regions for integer bootstrapping (IB) and 50,000 float solutions. Top: original ambiguities $\hat{\mathbf{a}}$ [cycles]; Bottom: \mathbf{Z} -decorrelated ambiguities $\hat{\mathbf{z}}$ [cycles].

283 The components of the bootstrapped estimator $\check{\mathbf{a}}_{\text{IB}}$ are given as

$$\begin{aligned}
 \check{a}_{n;\text{IB}} &= [\hat{a}_n] \\
 \check{a}_{j;\text{IB}} &= [\hat{a}_{j|J}] = \left[\hat{a}_j - \sum_{i=j+1}^n \underbrace{\sigma_{\hat{a}_j \hat{a}_{i|I}} \sigma_{\hat{a}_{i|I}}^{-2}}_{l_{i,j}} (\hat{a}_{i|I} - \check{a}_{i;\text{IB}}) \right], \quad (15) \\
 &\quad \forall j = 1, \dots, n-1
 \end{aligned}$$

284

285 The short-hand notation $\hat{a}_{i|I}$ stands for the i th ambiguity obtained through a con-
 286 ditioning on the previous $I = \{i + 1, \dots, n\}$ sequentially rounded ambiguities.
 287 The real-valued sequential least squares solution can be obtained by means of
 288 the triangular decomposition of the variance-covariance matrix of the ambigu-
 289 ties: $\mathbf{Q}_{\hat{a}\hat{a}} = \mathbf{L}^T \mathbf{D} \mathbf{L}$, where \mathbf{L} denotes a unit lower triangular matrix with entries $l_{i,j}$
 290 (see Eq.(15)) and \mathbf{D} a diagonal matrix with the conditional variances $\sigma_{\hat{a}_{i|I}}^2$ as its
 291 diagonal elements.

292 The pull-in regions for integer bootstrapping are given as:

$$293 \quad \mathcal{P}_{z, \text{IB}} = \{\mathbf{x} \in \mathbb{R}^n \mid |\mathbf{c}_i^T \mathbf{L}^{-T}(\mathbf{x} - \mathbf{z})| \leq \frac{1}{2}, i = 1, \dots, n\}, \mathbf{z} \in \mathbb{Z}^n \quad (16)$$

294 with \mathbf{c}_i the unit vector have a 1 as its i th entry and 0's otherwise.

295 Like rounding, bootstrapping suffers as well from a lack of \mathbf{Z} -invariance, i.e.
 296 $\check{\mathbf{z}}_{\text{IB}} \neq \mathbf{Z}^T \check{\mathbf{a}}_{\text{IB}}$ if $\hat{\mathbf{z}} = \mathbf{Z}^T \hat{\mathbf{a}}$. From Eq.(15) can be seen that changing the order will
 297 already result in a different outcome with bootstrapping.

298 Figure 4 shows a 2D example of the pull-in regions for integer bootstrapping,
 299 which in 2D are parallelograms. It can be clearly seen how bootstrapping is af-
 300 fected by the decorrelating \mathbf{Z} -transformation. Here 96% of the \mathbf{Z} -decorrelated
 301 float samples resides in $\mathcal{P}_{\mathbf{0}, \text{IB}}$ versus 29% of the original ambiguity samples.

302 3.4. Integer least squares

303 When solving the GNSS model of Eq.(3) in a least squares sense, but now with
 304 the additional constraint that the ambiguity parameters should be integer-valued,
 305 the integer estimator of the second step in the procedure becomes:

$$306 \quad \check{\mathbf{a}}_{\text{ILS}} = \arg \min_{\mathbf{z} \in \mathbb{Z}^n} \|\hat{\mathbf{a}} - \mathbf{z}\|_{\mathbf{Q}_{\hat{a}\hat{a}}}^2 \quad (17)$$

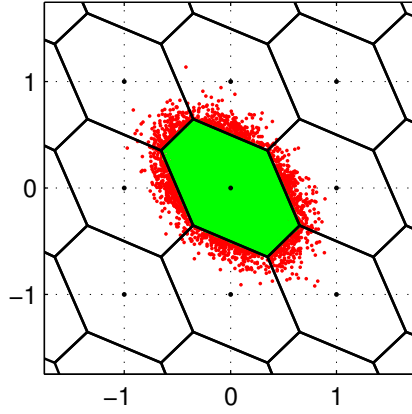
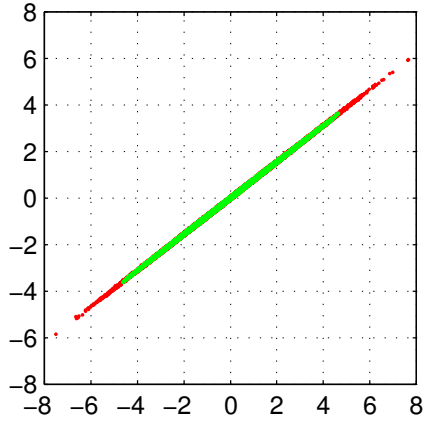


Figure 5: 2D pull-in regions for integer least squares (ILS) and 50,000 float solutions. Top: original ambiguities $\hat{\mathbf{a}}$ [cycles]; Bottom: \mathbf{Z} -decorrelated ambiguities $\hat{\mathbf{z}}$ [cycles].

307 with $\|\cdot\|_{\mathbf{Q}}^2 = (\cdot)^T \mathbf{Q}^{-1}(\cdot)$. The ILS pull-in region is defined by:

$$308 \quad \mathcal{P}_{z, \text{ILS}} = \{\mathbf{x} \in \mathbb{R}^n \mid |w| \leq \frac{1}{2} \|\mathbf{u}\|_{\mathbf{Q}_{\hat{\mathbf{a}}\hat{\mathbf{a}}}}, \forall \mathbf{u} \in \mathbb{Z}^n\} \quad (18)$$

309 with

$$310 \quad w = \frac{\mathbf{u}^T \mathbf{Q}_{\hat{\mathbf{a}}\hat{\mathbf{a}}}^{-1}(\mathbf{x} - \mathbf{z})}{\|\mathbf{u}\|_{\mathbf{Q}_{\hat{\mathbf{a}}\hat{\mathbf{a}}}}} \quad (19)$$

Table 2: Percentage of float solutions that is correctly fixed for the three integer estimation methods (corresponding to Figures 3 to 5).

	IR	IB	ILS
Original ambiguities $\hat{\mathbf{a}}$	23	29	97
\mathbf{Z} -decorrelated ambiguities $\hat{\mathbf{z}}$	95	96	97

311 the orthogonal projection of $(\mathbf{x} - \mathbf{z})$ onto the direction vector \mathbf{u} . Hence, $\mathcal{P}_{\mathbf{z},\text{ILS}}$ is
 312 the intersection of banded subsets centered at \mathbf{z} and having width $\|\mathbf{u}\|_{\mathbf{Q}_{\hat{\mathbf{a}}\hat{\mathbf{a}}}}$.

313 In contrast to integer rounding and integer bootstrapping, the ILS estimator is
 314 \mathbf{Z} -invariant: $\check{\mathbf{z}}_{\text{ILS}} = \mathbf{Z}^T \check{\mathbf{a}}_{\text{ILS}}$ if $\hat{\mathbf{z}} = \mathbf{Z}^T \hat{\mathbf{a}}$.

315 Figure 5 shows an example of the 2D pull-in regions for integer least squares.
 316 For the original VC-matrix $\mathbf{Q}_{\hat{\mathbf{a}}\hat{\mathbf{a}}}$ (top panel) the ILS pull-in region follows the dis-
 317 tribution of the float samples much better than in case of rounding and bootstrap-
 318 ping, compare with the corresponding Figures 3 and 4. Due to the \mathbf{Z} -invariance
 319 the percentage of float samples in $\mathcal{P}_{\mathbf{0},\text{ILS}}$ (the green dots) is 97% both for the orig-
 320 inal and \mathbf{Z} -decorrelated ambiguities. The percentages for all three integer estima-
 321 tors are summarized in Table 2.

322 An integer search is needed to determine $\check{\mathbf{a}}_{\text{ILS}}$. The ILS procedure is effi-
 323 ciently mechanized in the LAMBDA (Least squares AMBiguity Decorrelation
 324 Adjustment) method. A key element of the LAMBDA method is the decorrelating
 325 \mathbf{Z} -transformation, see Section 3.1, which results in largely reduced search times.
 326 For more information on the LAMBDA method and its wide-spread applications
 327 see e.g. (Teunissen, 1993, 1995b; Li and Teunissen, 2011; Chang et al., 2005;
 328 De Jonge and Tiberius, 1996; Hofmann-Wellenhof et al., 2001; Teunissen and
 329 Kleusberg, 1998; Leick, 2004; Strang and Borre, 1997; Misra and Enge, 2001).

330 **4. Success Rate: definition and evaluation tool**

331 In Section 2.3 the essence of correct integer estimation was described. It is
 332 thus important to have means available to evaluate the ambiguity success rate,
 333 i.e., the probability of correct integer estimation, P_s . This success rate is equal to
 334 the probability that $\hat{\mathbf{a}}$ resides in the correct pull-in region \mathcal{P}_a with \mathbf{a} the true but
 335 unknown ambiguity vector:

$$336 \quad P_s = P(\check{\mathbf{a}} = \mathbf{a}) = P(\hat{\mathbf{a}} \in \mathcal{P}_a) = \int_{\mathcal{P}_a} f_{\hat{\mathbf{a}}}(\mathbf{x}|\mathbf{a})d\mathbf{x} \quad (20)$$

337 The probability density function (PDF) of the float ambiguities, $f_{\hat{\mathbf{a}}}(\mathbf{x}|\mathbf{a})$, is as-
 338 sumed to be the normal PDF with mean \mathbf{a} :

$$339 \quad f_{\hat{\mathbf{a}}}(\mathbf{x}|\mathbf{a}) = \frac{1}{\sqrt{\det(2\pi\mathbf{Q}_{\hat{\mathbf{a}}\hat{\mathbf{a}})}}} \exp\{-\frac{1}{2}(\mathbf{x} - \mathbf{a})^T \mathbf{Q}_{\hat{\mathbf{a}}\hat{\mathbf{a}}}^{-1}(\mathbf{x} - \mathbf{a})\} \quad (21)$$

340 As the pull-in regions of the integer estimators are integer-translation invariant,
 341 the success rate can also be evaluated as:

$$342 \quad P_s = \int_{\mathcal{P}_0} f_{\hat{\mathbf{a}}}(\mathbf{x}|\mathbf{0})d\mathbf{x} \quad (22)$$

343 An illustration is given in Figure 6 for the ILS estimator: in the top panel the
 344 PDF of a 2D float ambiguity vector is shown, with the corresponding ILS pull-
 345 in regions underneath. The bottom panel shows the probability masses for each
 346 integer grid point, equal to the integral of the PDF over the corresponding pull-in
 347 regions. In this case, the success rate is equal to the probability mass at $[0 \ 0]^T$.

348 From the definition (22) it follows that the success rate depends on the integer
 349 estimation method (IR, IB or ILS) as well as on the float ambiguity precision
 350 captured by VC-matrix $\mathbf{Q}_{\hat{\mathbf{a}}\hat{\mathbf{a}}}$. From Eq.(4) follows that:

$$351 \quad \mathbf{Q}_{\hat{\mathbf{a}}\hat{\mathbf{a}}} = \left(\mathbf{A}^T \mathbf{Q}_{yy}^{-1} \mathbf{A} - \mathbf{A}^T \mathbf{Q}_{yy}^{-1} \mathbf{B} (\mathbf{B}^T \mathbf{Q}_{yy}^{-1} \mathbf{B})^{-1} \mathbf{B}^T \mathbf{Q}_{yy}^{-1} \mathbf{A} \right)^{-1} \quad (23)$$

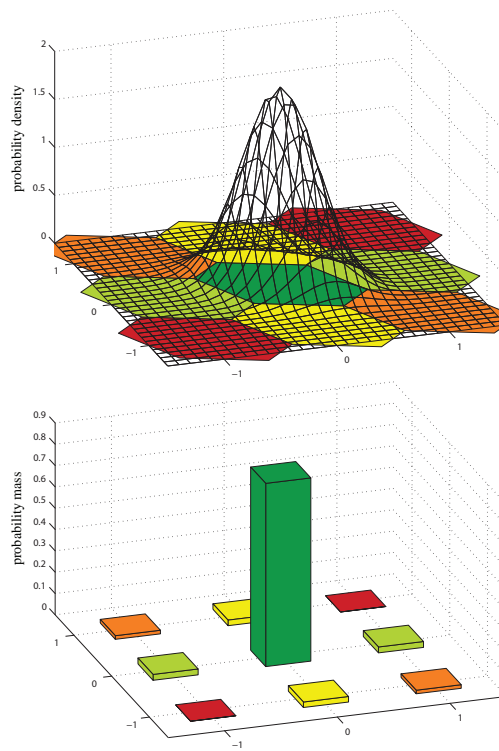


Figure 6: Top: PDF and 2D pull-in regions for ILS. Bottom: corresponding probability mass function.

Method	Option
1 ILS SRILS	1 AP : simulation SR_ILS_ap_sim
	3 (*) LB : IB exact SR_B_ex
	6 UB : ADOP SR_ILS_ub_adop
	2 AP : ADOP SR_ILS_ap_adop
	4 LB : region SR_ILS_lb_region
	7 UB : region SR_ILS_ub_region
	5 LB : VC-matrix SR_ILS_lb_vc
	8 UB : VC-matrix SR_ILS_ub_vc
2 IB SRBoot	1 (*) EXACT SR_B_ex
	2 UB : ADOP SR_ILS_ap_adop
3 IR SRRound	1 AP : simulation SR_R_ap_sim
	2 LB : VC-matrix SR_R_lb
	3 (*) UB : IB exact SR_B_ex

Figure 7: Ps-LAMBDA: overview of available methods and options in routine SuccessRate. Default option is indicated with (*). Names of underlying routines are shown as well. AP = approximation (blue), LB = lower bound (green), UB = upper bound (red).

352 From this it can be seen that the following factors drive the ambiguity float preci-
353 sion:

- 354 • receiver-satellite geometry (depends on time and location, as well as on
355 which GNSS is used) $\rightarrow \mathbf{B}, \mathbf{Q}_{yy}$
- 356 • measurement noise (depends on GNSS signal and receiver quality) $\rightarrow \mathbf{Q}_{yy}$
- 357 • assumptions on atmospheric delays (depends on atmosphere models and/or
358 between-receiver baseline length) $\rightarrow \mathbf{B}, \mathbf{Q}_{yy}$
- 359 • frequencies used (depends on GNSS and receiver) $\rightarrow \mathbf{A}$
- 360 • number of observation epochs $\rightarrow \mathbf{B}$

361 Note that the satellite geometry only affects \mathbf{Q}_{yy} if elevation-dependent weighting
362 is applied to the observations. The influence of the atmosphere delays depends on
363 whether the delays are estimated and thus included as unknown parameters in \mathbf{b} ,
364 and what uncertainty is assigned to the corrections if applied.

365 Since the success rate can be computed once the float ambiguity VC-matrix
366 $\mathbf{Q}_{\hat{a}\hat{a}}$ is known, it can be computed without the need for actual data. As such, the
367 success rate can be used as a very important performance measure for:

368

- 369 • planning purposes (design computations): what is the performance to be
370 expected given a certain measurement set-up at a given time and location;
- 371
- 372 • deciding whether or not to fix the ambiguities to the integer estimates dur-
373 ing the actual data processing (in real-time or post-processing mode);

374

- 375 • research purposes, e.g. to study the impact of receiver noise characteristics,
376 availability of more signals / satellites, baseline length, etcetera.

377

378 As mentioned, the success rates also depend on the selected integer estimation
379 method, since the pull-in region is different for IR, IB and ILS. In (Teunissen,
380 1999a) it was proven that:

$$381 \quad P(\check{\mathbf{a}}_{\text{IR}} = \mathbf{a}) \leq P(\check{\mathbf{a}}_{\text{IB}} = \mathbf{a}) \leq P(\check{\mathbf{a}}_{\text{ILS}} = \mathbf{a}) \quad (24)$$

382 The ordering is thus the same as the ordering in terms of complexity, since IR
383 is the simplest and ILS the most complex method. This means that if IR or IB
384 provides a very sharp lower bound, a user could decide to use the simpler integer
385 estimation method if their success rate is close to 1 and still obtain (close to)
386 optimal performance.

387 The success rate cannot be evaluated exactly in all cases due to the complex
388 integration over the pull-in region. It is of course important to be able to have
389 good approximations of the success rate in case exact evaluation is not feasible.
390 A lower bound is an approximation of the success rate, which is guaranteed to be
391 smaller than or equal to the actual success rate. As such it is particularly useful.
392 However, if the lower bound is not tight, this may result in a unnecessarily high
393 rejection rate as the success rate is deemed too low. An upper bound can be useful
394 as well, especially in combination with a lower bound, since it then tells the user
395 in which range the success rate will be. If the upper bound is below a user-defined
396 threshold, one cannot expect ambiguity resolution to be successful. In addition,
397 for IR and IB it may be useful to have an upper bound which is invariant for the
398 class of admissible ambiguity transformations.

399 Different approximations and bounds were proposed in literature, an evalua-
 400 tion of some of the bounds was made in (Verhagen, 2005; Thomsen, 2000). All
 401 bounds and approximations are now implemented in a newly developed Matlab
 402 toolbox, called Ps-LAMBDA. Figure 7 gives an overview of the structure. The
 403 main routine is `SuccessRate` which needs as input:

`Qa` the VC-matrix of the float ambiguities $Q_{\hat{a}\hat{a}}$
`method` 1 = ILS [DEFAULT], 2 = IB, 3 = IR
`option` the approximation / bound to compute
 (see Figure 7)
 404 `decor` 1 = decorrelation [DEFAULT]
 0 = no decorrelation
`nsamp` number of samples
 only used for simulation-based approximation
 405

406 The choice for `decor` is only relevant for IR and IB, since these estimators are
 407 not \mathbf{Z} -invariant. Decorrelation is always applied for ILS to ensure computational
 408 efficiency.

409 The toolbox also includes a Graphical User Interface which allows the user
 410 to select an input file which contains the VC-matrix $Q_{\hat{a}\hat{a}}$ and to compute all the
 411 desired bounds and approximations for different integer estimation methods si-
 412 multaneously.

413 In the next section the bounds and approximations for each of the three esti-
 414 mators are presented. The performance of the bounds and approximations will be
 415 assessed for different GNSS models, where the different factors affecting the float
 416 ambiguity precision are varied as shown in Table 3. An exponential elevation-
 417 dependent weighting is applied (more noise is assumed for observations from

Table 3: Measurement scenarios used in Section 5 (standard deviations apply to zenith direction).

system	GPS - combined GPS+Galileo
times	49 different epochs
frequencies	L5 - L1+L5 - L1+L5+L2/E5b
standard deviations of undifferenced observations	code: 15 cm phase: 1 mm
VC-matrix scale factors	0.25 - 0.5 - 1 - 2 - 4
standard deviation of ionosphere corrections	5 - 15 mm

418 low-elevation satellites) to the standard deviations of the observations and of the
419 ionosphere corrections. The scale factors applied to the VC-matrix $\mathbf{Q}_{\hat{a}\hat{a}}$ can ei-
420 ther be interpreted as representing a different number of epochs, or a different
421 measurement precision due to different receiver quality.

422 5. Success Rate: bounds and approximations

423 5.1. Approximation based Monte Carlo simulations

424 The success rate of integer estimation can be approximated by means of Monte
425 Carlo simulation. The procedure is as follows. It is assumed that the float solution
426 is normally distributed $\hat{\mathbf{a}} \sim N(\mathbf{a}, \mathbf{Q}_{\hat{a}\hat{a}})$, and thus the distribution is symmetric about
427 the mean \mathbf{a} . Hence, we may shift the distribution over \mathbf{a} and draw samples from
428 the distribution $N(\mathbf{0}, \mathbf{Q}_{\hat{a}\hat{a}})$.

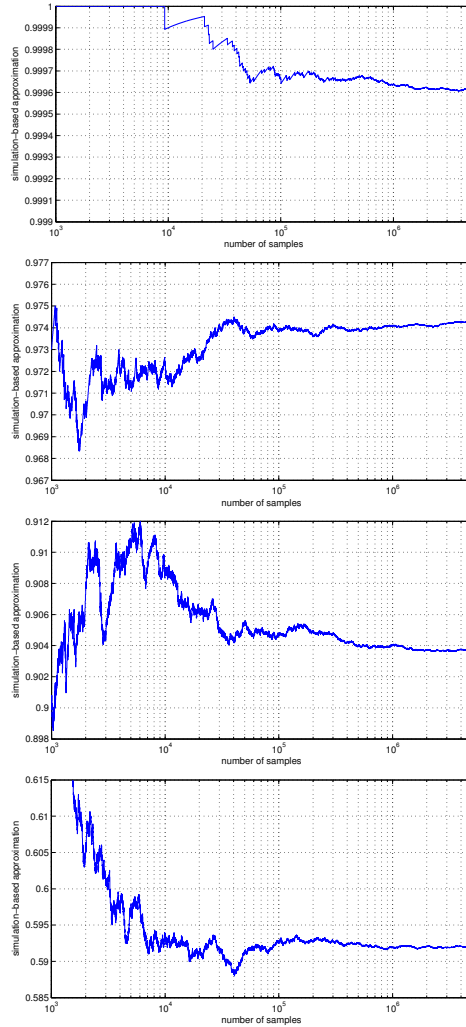


Figure 8: Examples of simulation-based success rate as function of number of samples. Each panel shows the results for a different GNSS model.

429 The first step is to use a random generator to generate n independent samples
 430 from the univariate standard normal distribution $N(0, 1)$, and then collect these in
 431 a vector s . This vector is transformed by means of $\hat{\mathbf{a}} = \mathbf{G}s$, with \mathbf{G} equal to the
 432 Cholesky factor of $\mathbf{Q}_{\hat{\mathbf{a}}\hat{\mathbf{a}}} = \mathbf{G}\mathbf{G}^T$. The result is a sample $\hat{\mathbf{a}}$ from $N(\mathbf{0}, \mathbf{Q}_{\hat{\mathbf{a}}\hat{\mathbf{a}}})$, and

433 this sample is used as input for integer estimation. If the output of this estimator
434 equals the null vector, then it is correct, otherwise it is incorrect. This process can
435 be repeated an N number of times, and one can count how many times the null
436 vector is obtained as a solution, say N_s times. The approximation of the success
437 rate follows then as:

$$438 \quad P_s \approx \frac{N_s}{N} \quad (25)$$

439 In order to get good approximations, the number of samples N must be sufficiently
440 large (Teunissen, 1998a). The disadvantage is that it may be very time-consuming
441 to evaluate Eq.(25), especially in case of ILS, since for each sample an integer
442 search is required.

443 The concept of approximating the success rate based on simulations was al-
444 ready applied in Sections 3.2-3.4, see Table 2.

445 Figure 8 shows for four GNSS models how the approximation performs de-
446 pending on the number of samples used (similar results were obtained for many
447 other GNSS positioning models). It follows that at least 10^5 samples should be
448 used to get a good approximation. At the same time it can be seen that using more
449 samples generally only has a small effect, in the order of 10^{-3} , especially in cases
450 where the success rate is close to 1. With 10^6 samples the approximation will be
451 very close to the true value. In the remainder of this contribution the simulation-
452 based success rates will be compared to other bounds and approximations. The
453 number of samples used is 10^6 .

454 Ps-LAMBDA allows to evaluate the simulation-based success rates for IR and
455 ILS (option 1 in Figure 7), where the user may specify the number of samples to
456 be used. The option is not available for IB, as its success rate can be evaluated
457 exactly, as will be shown in Section 5.3.

458 *5.2. Integer Rounding success rates*

459 The n -fold integral over the IR pull-in region defined in (14) is difficult to
 460 evaluate. Only if the VC-matrix $\mathbf{Q}_{\hat{a}\hat{a}}$ is diagonal will the success rate become
 461 equal to the n -fold product of the univariate success rates. In (Teunissen, 1998b)
 462 it was shown that this also provides a lower bound in case $\mathbf{Q}_{\hat{a}\hat{a}}$ is not diagonal:

$$463 \quad P_{s,\text{IR}} = P(\check{\mathbf{a}}_{\text{IR}} = \mathbf{a}) \geq \prod_{i=1}^n \left(2\Phi\left(\frac{1}{2\sigma_{\hat{a}_i}}\right) - 1 \right) \quad (26)$$

464 with $\Phi(x)$ the cumulative normal distribution function:

$$465 \quad \Phi(x) = \frac{1}{\sqrt{2\pi}} \int_{-\infty}^x \exp\left\{-\frac{1}{2}t^2\right\} dt$$

466 In Section 3.2 it was mentioned that IR is not \mathbf{Z} -invariant. This holds for
 467 the IR success rates as well, since the pull-in regions are unaffected by a \mathbf{Z} -
 468 transformation, while the distribution of the transformed ambiguities is changed
 469 to $\hat{\mathbf{z}} \sim N(\mathbf{Z}^T \mathbf{a}, \mathbf{Q}_{\hat{\mathbf{z}}\hat{\mathbf{z}}})$. If IR is applied to the \mathbf{Z} -decorrelated ambiguities, the success
 470 rate will increase due to the improved precision of the decorrelated ambiguities,
 471 i.e.

$$472 \quad P(\check{\mathbf{z}}_{\text{IR}} = \mathbf{z}) \geq P(\check{\mathbf{a}}_{\text{IR}} = \mathbf{a}) \quad (27)$$

473 According to Eq.(24), IB will always result in a success rate higher than or
 474 equal to the IR success rate if the same parameterization of the float ambiguities
 475 is used. Hence, the IB success rate can be used as an upper bound for IR. In the
 476 next subsection it will be shown that the IB success rate can in fact be evaluated
 477 exactly.

478 Figure 9 shows the lower bound and upper bound versus the actual IR success
 479 rates (all for the decorrelated ambiguities). It can be seen that the lower bound
 480 is very tight, whereas the upper bound based on the IB success rate is not as

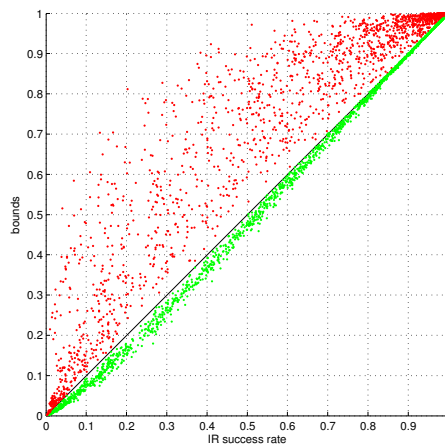


Figure 9: IR success rates: upper bound based on IB (red) and lower bound based on diagonal VC-matrix (green) versus the actual IR success rate for the models from Table 3.

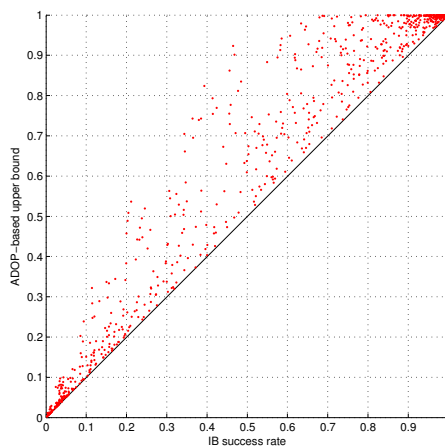


Figure 10: IB success rates: ADOP-based upper bound versus the exact IB success rate for the models from Table 3.

481 tight, thus indicating that integer bootstrapping may still significantly outperform
 482 integer rounding.

483 *5.3. Integer Bootstrapping success rates*

484 In case of bootstrapping the success rate can be evaluated exactly using (Teu-
485 nissen, 1998b):

$$486 \quad P_{s,IB} = P(\check{\mathbf{a}}_{IB} = \mathbf{a}) = \prod_{i=1}^n \left(2\Phi\left(\frac{1}{2\sigma_{\hat{a}_{i|l}}}\right) - 1 \right) \quad (28)$$

487 The IB success rate is not \mathbf{Z} -invariant. Bootstrapping may perform close to op-
488 timal if applied to the decorrelated ambiguities $\hat{\mathbf{z}}$, (Teunissen, 1998b; Verhagen,
489 2005), and as with rounding we have:

$$490 \quad P(\check{\mathbf{z}}_{IB} = \mathbf{z}) \geq P(\check{\mathbf{a}}_{IB} = \mathbf{a}) \quad (29)$$

491 For bootstrapping we thus have an exact and easy-to-compute formula for the
492 success rate. Still it can be useful to have an upper bound, which is \mathbf{Z} -invariant,
493 since if this upper bound is too small, it can be immediately concluded that neither
494 bootstrapping, nor rounding, will be successful for *any* parameterization of the
495 ambiguities. In Teunissen (2000) it was proven that such an upper bound is given
496 by:

$$497 \quad P_{s,IB} \leq \left(2\Phi\left(\frac{1}{2ADOP}\right) - 1 \right)^n \quad (30)$$

498 with ADOP being the Ambiguity Dilution of Precision given by:

$$499 \quad ADOP = \sqrt{\det(\mathbf{Q}_{\hat{\mathbf{a}}\hat{\mathbf{a}}})^{\frac{1}{n}}} \quad (31)$$

500 with units of *cycles*. The ADOP is a diagnostic that captures the main char-
501 acteristics of the ambiguity precision. It was introduced in (Teunissen, 1997),
502 described and analyzed in (Teunissen and Odijk, 1997; Odijk and Teunissen,
503 2008) and is widely used, see the introduction of (Odijk and Teunissen, 2008).
504 The ADOP is invariant for the class of admissible ambiguity transformation, i.e.

505 $\det(\mathbf{Q}_{\hat{a}\hat{a}}) = \det(\mathbf{Q}_{\hat{z}\hat{z}})$. When the ambiguities are completely decorrelated, the
 506 ADOP equals the geometric mean of the standard deviations of the ambiguities,
 507 hence it can be considered as a measure of the average ambiguity precision.

508 Figure 10 shows that the upper bound is in these cases often significantly
 509 higher than the exact success rate $P(\check{\mathbf{z}}_{\text{IB}} = \mathbf{z})$. Better bounding performance is
 510 obtained for lower dimensions n , which is due to the replacement of the n condi-
 511 tional standard deviations in Eq.(28) by a single value equal to ADOP.

512 5.4. Integer Least Squares success rates

513 Due to the complex geometry of the ILS pull-in region defined in Eq.(18),
 514 the multivariate integral in Eq.(22) can only be evaluated by using Monte Carlo
 515 simulation. In addition, several lower and upper bounds of the ILS success rate
 516 have been proposed. They will all be presented here.

517 *Bounds and approximations based on IB and ADOP*

518 Teunissen (1999a) proved that the ILS estimator is optimal, in the sense that it
 519 gives the maximum success rate. Furthermore, it was already mentioned that IB
 520 may perform close to optimal if applied to decorrelated ambiguities. Therefore the
 521 corresponding IB success rate can be used as a lower bound for the ILS success
 522 rate:

$$523 \quad P_{s,\text{ILS}} = P(\check{\mathbf{a}}_{\text{ILS}} = \mathbf{a}) \geq \prod_{i=1}^n \left(2\Phi\left(\frac{1}{2\sigma_{\hat{z}_{i|l}}}\right) - 1 \right) \quad (32)$$

524 The conditional standard deviations $\sigma_{\hat{z}_{i|l}}$ of the decorrelated ambiguities must be
 525 used (see Eq.(29)).

526 Consequently, the invariant upper bound of the IB success rate from Eq.(30)
 527 may serve as an approximation of the ILS success rate.

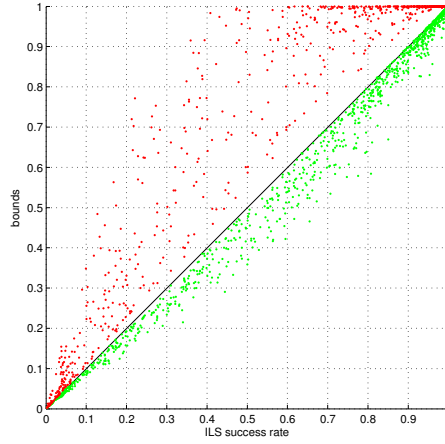


Figure 11: ILS success rates: lower bound based on IB (green) and upper bound based on ADOP (red) versus the actual ILS success rate for the models from Table 3.

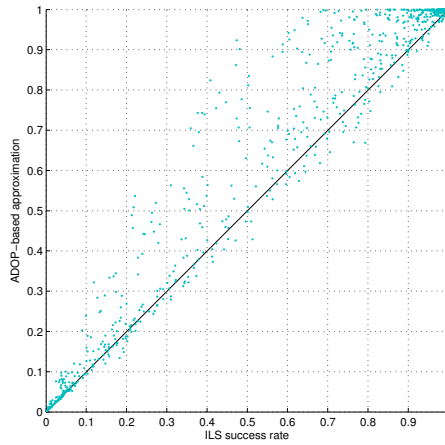


Figure 12: ILS success rates: ADOP-based approximation versus the actual ILS success rate for the models from Table 3.

528 Furthermore, an upper bound for the ILS success rate based on the ADOP can
 529 be given as:

530
$$P_{s, \text{ILS}} \leq P\left(\chi^2(n, 0) \leq \frac{c_n}{ADOP^2}\right) \quad (33)$$

531 with

$$532 \quad c_n = \frac{\left(\frac{n}{2}\Gamma\left(\frac{n}{2}\right)\right)^{\frac{2}{n}}}{\pi}$$

533 This bound was introduced in Hassibi and Boyd (1998), while the proof was given
534 in Teunissen (2000).

535 Figure 11 shows how the IB success rate performs as a lower bound for ILS. In
536 practice, the IB success rate is commonly used as the best known lower bound, and
537 these results confirm that especially if the success rate is high, this is indeed the
538 case. At the same time, it can be seen how ILS may still significantly outperform
539 IB for lower success rates.

540 Figure 11 shows that for these cases the ADOP-based upper bound often gives
541 a too optimistic value compared to the actual success rate. As is shown later,
542 however, the bounding performance improves for lower dimensions (cf. Figure
543 17).

544 A similar conclusion can be given for the ADOP-based approximation of the
545 ILS success rate as shown in Figure 12. Only in some of these cases can it be
546 used as a coarse approximation. The approximation improves in case of lower
547 dimensions (cf. Figure 17).

548 *Bounds based on bounding the integration region*

549 In (Teunissen, 1998a) lower and upper bounds for the ILS success rate were
550 obtained by bounding the integration region. Obviously, a lower bound is obtained
551 if the integration region is chosen such that it is completely contained by the pull-
552 in region, and an upper bound is obtained if the integration region is chosen such
553 that it completely contains the pull-in region. The integration region can then be
554 chosen such that the integral is easy-to-evaluate. In *ibid* the integration region for

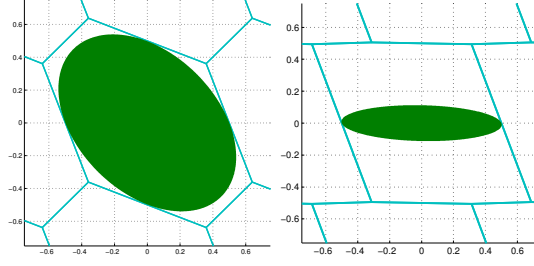


Figure 13: Two examples of the ellipsoidal region (green) contained by the pull-in region $\mathcal{P}_{0,\text{ILS}}$ (different shape of pull-in regions is due to different VC-matrices $\mathbf{Q}_{\hat{z}\hat{z}}$).

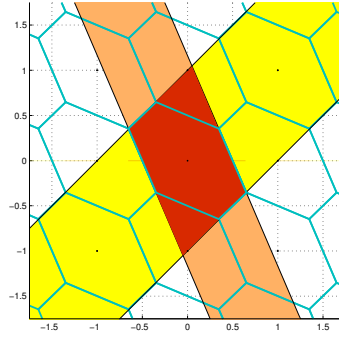


Figure 14: Integration region (red) containing $\mathcal{P}_{0,\text{ILS}}$ and defined by the intersection of two banded subsets.

555 the lower bound is chosen as an ellipsoidal region $E_a \subset \mathcal{P}_{a,\text{ILS}}$. The probability
 556 $P(\hat{\mathbf{a}} \in E_a)$ can be evaluated based on the χ^2 -distribution:

$$557 \quad P_{s,\text{ILS}} \geq P(\hat{\mathbf{a}} \in E_a) = P\left(\chi^2(n, 0) \leq \frac{1}{4} \min_{\mathbf{u} \in \mathbb{Z}^n \setminus \{0\}} \|\mathbf{u}\|_{\mathbf{Q}_{\hat{a}\hat{a}}}^2\right) \quad (34)$$

558 The concept is illustrated in Figure 13 for two different pull-in regions, corre-
 559 sponding to different VC-matrices $\mathbf{Q}_{\hat{z}\hat{z}}$.

560 The upper bound can thus be obtained by defining a region $U_a \supset \mathcal{P}_{a,\text{ILS}}$. Given
 561 the definition of the ILS pull-in region $\mathcal{P}_{a,\text{ILS}}$ in Eq.(18), it follows that any finite
 562 intersection of $p < n$ banded subsets defined by w of Eq.(19) will enclose $\mathcal{P}_{a,\text{ILS}}$.
 563 The idea is illustrated in Figure 14 for the 2D case where U_a is chosen as the

564 intersection of two banded subsets. The probability $P(\hat{\mathbf{a}} \in U_a)$, however, cannot
 565 be evaluated exactly either, but can be bounded from above to obtain (Teunissen,
 566 1998a):

$$567 \quad P_{s,\text{ILS}} \leq P(\hat{\mathbf{a}} \in U_a) \leq \prod_{i=1}^p \left(2\Phi\left(\frac{1}{2\sigma_{v_{i|l}}}\right) - 1 \right) \quad (35)$$

568 with the conditional standard deviation $\sigma_{v_{i|l}}$ of vector \mathbf{v} . These are equal to the
 569 square root of the diagonal elements of \mathbf{D} from the $\mathbf{L}^T \mathbf{D} \mathbf{L}$ -decomposition of $\mathbf{Q}_{\mathbf{v}\mathbf{v}}$
 570 with its elements given by:

$$571 \quad \sigma_{v_i v_j} = \frac{\mathbf{u}_i^T \mathbf{Q}_{\hat{\mathbf{a}}\hat{\mathbf{a}}}^{-1} \mathbf{u}_j}{\|\mathbf{u}_i\|_{\mathbf{Q}_{\hat{\mathbf{a}}\hat{\mathbf{a}}}} \|\mathbf{u}_j\|_{\mathbf{Q}_{\hat{\mathbf{a}}\hat{\mathbf{a}}}}}, \quad \mathbf{u}_i, \mathbf{u}_j \in \mathbb{Z}^n$$

572 where the \mathbf{u}_i , $i = 1, \dots, p$ need to be linearly independent. How to evaluate this
 573 upper bound is described in (Teunissen, 1998a; Verhagen, 2005). Note that in the
 574 higher dimensional case many subsets are necessary to obtain a tight upper bound,
 575 and selection of the subset is rather complicated. In addition, it is computationally
 576 demanding, since the determination of the subset involves the evaluation of many
 577 integer candidates to be obtained with LAMBDA.

578 Kondo (2003) presented a lower bound of the ILS success rate by replacing
 579 the conditional standard deviation $\sigma_{v_{i|l}}$ in Eq.(35) by the unconditional standard
 580 deviation σ_{v_i} . In Verhagen (2005) it was explained that this is only guaranteed to
 581 be a lower bound under certain conditions, which are difficult to fulfill.

582 Figure 15 shows the lower and upper bound of the ILS success rate based on
 583 bounding the integration region. It can be seen that the upper bound performs
 584 reasonably well, whereas the lower bound is generally not tight at all - it will be
 585 close to zero unless the success rate is very close to 1. The bad performance can
 586 be explained based on the 2D example on the right-hand side of Figure 13: the
 587 ellipsoidal region may leave a large part of the ILS pull-in region uncovered. This

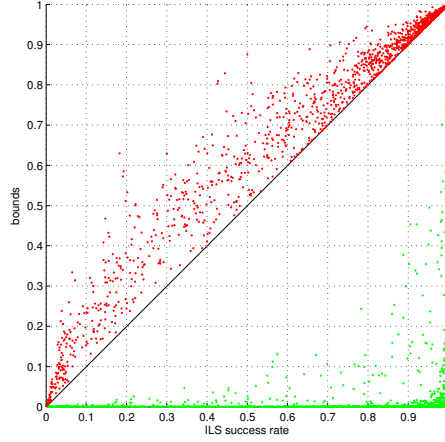


Figure 15: ILS success rates: lower and upper bounds based on bounding the integration region versus the actual ILS success rate for the models from Table 3.

588 will be the case when there is a large variation in the variances $\sigma_{\hat{z}_i \hat{z}_i}$ (making the
 589 ellipsoidal region elongated).

590 *Bounds based on bounding the VC-matrix*

591 It is also possible to obtain a lower and an upper bound by bounding the ac-
 592 tual VC-matrix from above and below by diagonal matrices, and then to compute
 593 the probability of correct integer estimation belonging to these diagonal matrices,
 594 (Teunissen, 1998a). The simplest way is to bound the actual VC-matrix with:

595
$$\lambda_{\min} \mathbf{I}_n \leq \mathbf{Q}_{\hat{z}\hat{z}} \leq \lambda_{\max} \mathbf{I}_n \quad (36)$$

596 where λ_{\min} and λ_{\max} are the minimum and maximum eigenvalues of $\mathbf{Q}_{\hat{z}\hat{z}}$, and \mathbf{I}_n is
 597 an identity matrix of order n . The ILS success rate bounds follow as:

598
$$\left(2\Phi\left(\frac{1}{2\sqrt{\lambda_{\max}}}\right) - 1\right)^n \leq P_{s,\text{ILS}} \leq \left(2\Phi\left(\frac{1}{2\sqrt{\lambda_{\min}}}\right) - 1\right)^n \quad (37)$$

599 Figure 16 shows the lower and upper bound of the ILS success rate based
 600 on bounding the VC-matrix. It can be seen that both bounds perform poorly.

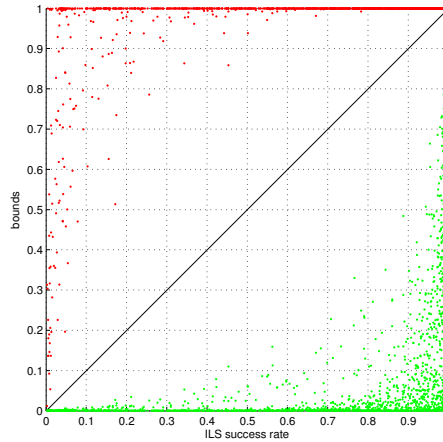


Figure 16: ILS success rates: lower and upper bounds based on bounding the VC-matrix versus the actual ILS success rate for the models from Table 3.

601 Similarly as with the ADOP-based approximation of the ILS success rate, this is
 602 especially true for large n due to the replacement of the n conditional standard
 603 deviations in Eq.(32) by the square root of the minimum or maximum eigenvalue,
 604 respectively.

605 *Examples with other models*

606 So far, the performance of the success rate bounds and approximations was
 607 analyzed based on the linearized DD GNSS model parameterized in terms of the
 608 baseline unknowns. However, it is also possible to use the observation equations
 609 (1) directly, and hence parameterize the DD model in terms of the satellite-receiver
 610 ranges. This model is referred to as the geometry-free model, and is used for
 611 example for integrity monitoring or as a first step in the data processing. Here, we
 612 will show an example based on a dual-frequency GNSS model for one satellite-
 613 receiver pair (i.e. one DD code and phase observation per frequency). The GPS
 614 L1 and L2 frequencies, see Table 1, have been considered. The undifferenced

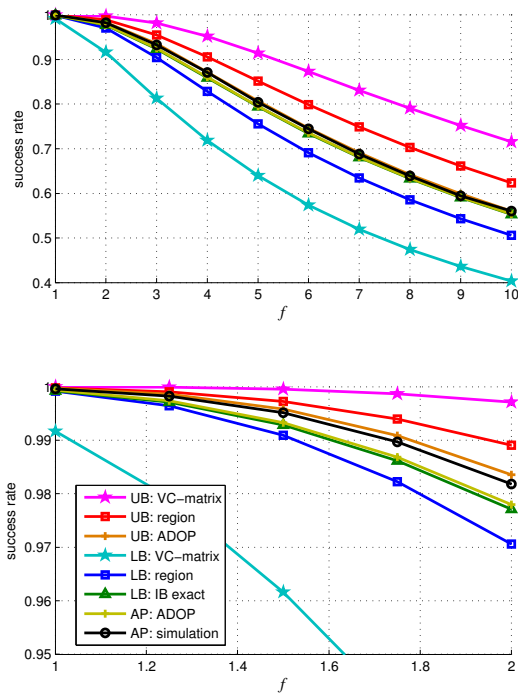


Figure 17: ILS success rate bounds for 2-frequency geometry-free model with 2 ambiguities, f is the scale factor applied to the VC-matrix (bottom panel shows same results, but only for smaller f).

615 code and phase standard deviations were set to 15 cm and 1.5 mm, respectively.
 616 The float ambiguity VC-matrix (units are *cycles*²) obtained in this way is:

$$617 \quad \mathbf{Q}_{\hat{a}\hat{a}} = \begin{bmatrix} 1.2429 & 0.9683 \\ 0.9683 & 0.7547 \end{bmatrix} \quad (38)$$

618 In addition, a scaling is applied to analyze the performance for different preci-
 619 sions:

$$620 \quad \mathbf{Q}_{\hat{a}\hat{a},f} = f \times \mathbf{Q}_{\hat{a}\hat{a}} \quad (39)$$

621 The ILS success rate approximations and bounds are shown in Figure 17 as a
 622 function of the scale factor f . The lower bound based on the exact IB success rate
 623 is very sharp. Interestingly, this also holds for the ADOP-based upper bound and
 624 approximation (the orange line is hardly visible, as it is plotted below the graph of
 625 the simulation-based success rate). In this case the bounds based on bounding the
 626 integration region are quite sharp if the success rate is high, but become less tight
 627 as the scale factor increases, and consequently the success rate decreases.

628 In all results shown so far, the bounds based on bounding the VC-matrix $\mathbf{Q}_{\hat{a}\hat{a}}$
 629 are generally not tight at all. An example where also these bounds will work well
 630 is when all variances are equal to a certain value v and all the covariances equal to
 631 a value c , with $v \gg c$:

$$632 \quad \sigma_{\hat{a}_i\hat{a}_i}^2 = v, \quad \sigma_{\hat{a}_i\hat{a}_j} = c, \quad \forall i, j = 1, \dots, n; \quad i \neq j \quad (40)$$

633 Figure 18 shows the bounds for an example with $n = 2$, $v = 0.02$ and $c = 0.0005$.
 634 Again the scaling according to Eq.(39) is applied.

635 *Which bounds or approximations to use?*

636 The results in this section show that the success rate bounds and approxima-
 637 tions differ in their performance. The simulation-based approximations of the IR

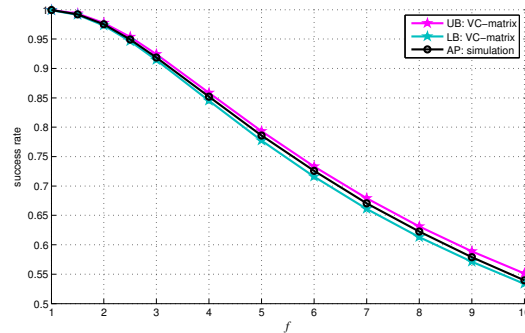


Figure 18: ILS success rate bounds based on bounding the (2×2) scaled VC-matrix with both variances equal to 0.02, and covariance equal to 0.0005. The scale factor is equal to f .

638 and ILS success rates work well if enough samples are used. However, they may
 639 not be suitable for real-time applications as their computation time may be long.
 640 Computation time will also be an issue for real-time applications if the upper
 641 bound of the ILS success rate based on bounding the integration is considered.
 642 For design and research purposes, as well as for post-processing, computation
 643 time will not be an issue. All other bounds and approximations can be used in
 644 real-time.

645 For the IR success rate, the lower bound was shown to perform well. For
 646 the ILS success rate, the lower bound based on the exact IB success rate, and
 647 the upper bound based on bounding the integration region generally perform very
 648 well for the GNSS models considered here. Furthermore, it was shown that the
 649 other bounds and approximations may work well for certain applications where
 650 the dimension is lower or the structure of the VC-matrix $Q_{\hat{a}\hat{a}}$ is different, see for
 651 example Figures 17 and 18.

652 **6. Success rates with GPS, Galileo and Compass**

653 As an example on how the Ps-LAMBDA toolbox can be used to assess the (po-
654 tential) performance of GNSS, a comparative study will be presented for different
655 GNSSs. Such a study is useful to:

- 656 • study the performance as obtained with the actual constellations for GPS
657 and Compass;
- 658 • investigate what the potential of Galileo is, both as a stand-alone system or
659 combined with GPS. The full nominal Galileo constellation (as planned) is
660 used.

661 The current constellation of Galileo comprises only four satellites, and is therefore
662 not considered in this study.

663 Here, the ILS success rates are evaluated for 25 different times on 22-March-
664 2012, 0:00 - 12:00 UTC, for a 35km baseline in Perth, Australia. The same as-
665 sumptions for noise as in Table 3 are used for all signals. The standard deviation
666 of the zenith ionosphere corrections is 15mm, zenith troposphere delays are esti-
667 mated. The following signals, see Table 1, are considered:

- 668 • GPS L1+L5;
- 669 • Galileo L1+L5;
- 670 • Compass B1+B2;
- 671 • GPS+Galileo L1+L5/E5a.

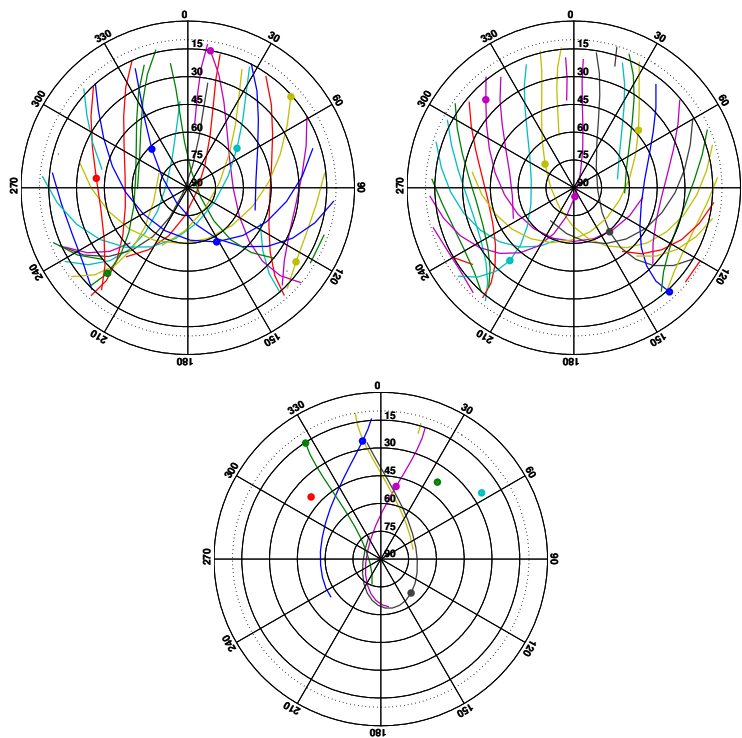


Figure 19: Skyplots of GPS (left), Galileo (middle) and Compass (right) for Perth, Australia on 22-March-2012, 0:00 - 12:00 UTC. The plots show the azimuth [deg] and elevation [deg] of the satellites; the dots correspond to the satellite positions at 6:00 UTC.

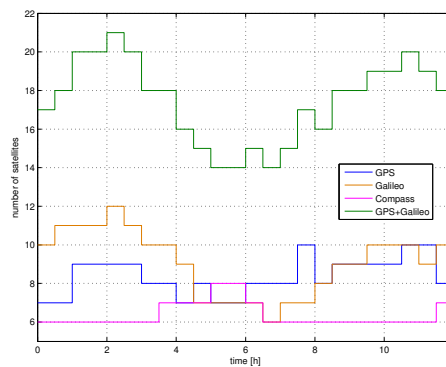


Figure 20: Number of visible satellites in Perth, Australia on 22-March-2012, 0:00 - 12:00 UTC.

672 Using almanac data for each of the GNSSs, satellite positions can be computed
673 and the matrices \mathbf{A} and \mathbf{B} in model (3) can be constructed, as well as the corre-
674 sponding VC-matrix \mathbf{Q}_{yy} . Figure 19 shows the skyplots for the three considered
675 constellations. Note that during this time window three geostationary satellites
676 and five Inclined Geo-Synchronous Orbit satellites of Compass were visible. The
677 GPS and Galileo constellations comprise of 32 and 30 Medium Earth Orbiting
678 satellites at inclinations of 55 and 56 degrees, respectively. This explains the dif-
679 ferences in Figure 19. Figure 20 shows the number of visible satellites as function
680 of time for each system.

681 Figure 21 reports the following bounds and approximation of the ILS success
682 rate: the lower bound based on IB, the upper bound based on bounding the in-
683 tegration region, and the simulation-based approximation with 10^6 samples. The
684 top and bottom panels show the single-epoch and four-epoch results, respectively.
685 The single-epoch success rates are much lower (note the different scales in the
686 bottom and top panels), and then the bounds are not as tight. However, when us-
687 ing 4 epochs of observations the success rates will improve significantly and also
688 the bounds become much sharper.

689 These results can now be used to analyze and compare the performance of the
690 different GNSSs.

691 *Satellite geometry and number of epochs*

692 In Section 4 an overview of the factors affecting the success rate was given.
693 The results in Figure 21 clearly show some of these dependencies:

- 694 • Receiver-satellite geometry: success rates are generally higher if more satel-
695 lites are visible, compare e.g. the number of visible Galileo satellites as

696 function of time in Figure 20 with the 1-epoch success rates in Figure 21.
697 However, even with the same number of visible satellites, the success rate
698 may strongly fluctuate. See for example the results obtained for Compass:
699 from 0:00 - 3:30 UTC six satellites are visible, but the 1-epoch success rate
700 varies between 0.57 and 0.71. This is due to the dependence of the success
701 rate on the receiver-satellite geometry, since all other factors affecting the
702 success rate remain the same.

- 703 • Number of observation epochs: more epochs will result in much improved
704 success rates, as is clear by comparing the results from the top and bottom
705 panels.

706 The dependency on measurement noise is not explicitly analyzed here, but the
707 effect will be similar as when changing the number of observation epochs.

708 *Choice of GNSS*

709 For this scenario, GPS and Galileo would give similar performance. At times
710 where more Galileo satellites are visible, the success rates with Galileo tend to
711 be higher, as expected. Combined GPS+Galileo brings a great potential, as it
712 significantly outperforms the single GNSSs.

713 The current Compass constellation provides on average 6 to 7 visible satellites
714 at this location, which is generally lower than with the current GPS constellation.
715 This causes the success rates to be lower on average. In addition, the receiver-
716 satellite geometry contributes to the lower success rates as well, since for Compass
717 the satellite visibility is restricted to a smaller portion of the sky, as can be seen in
718 Figure 19; with GPS and Galileo the satellites from Eastern and Western directions
719 at different elevations will contribute to a better geometry.

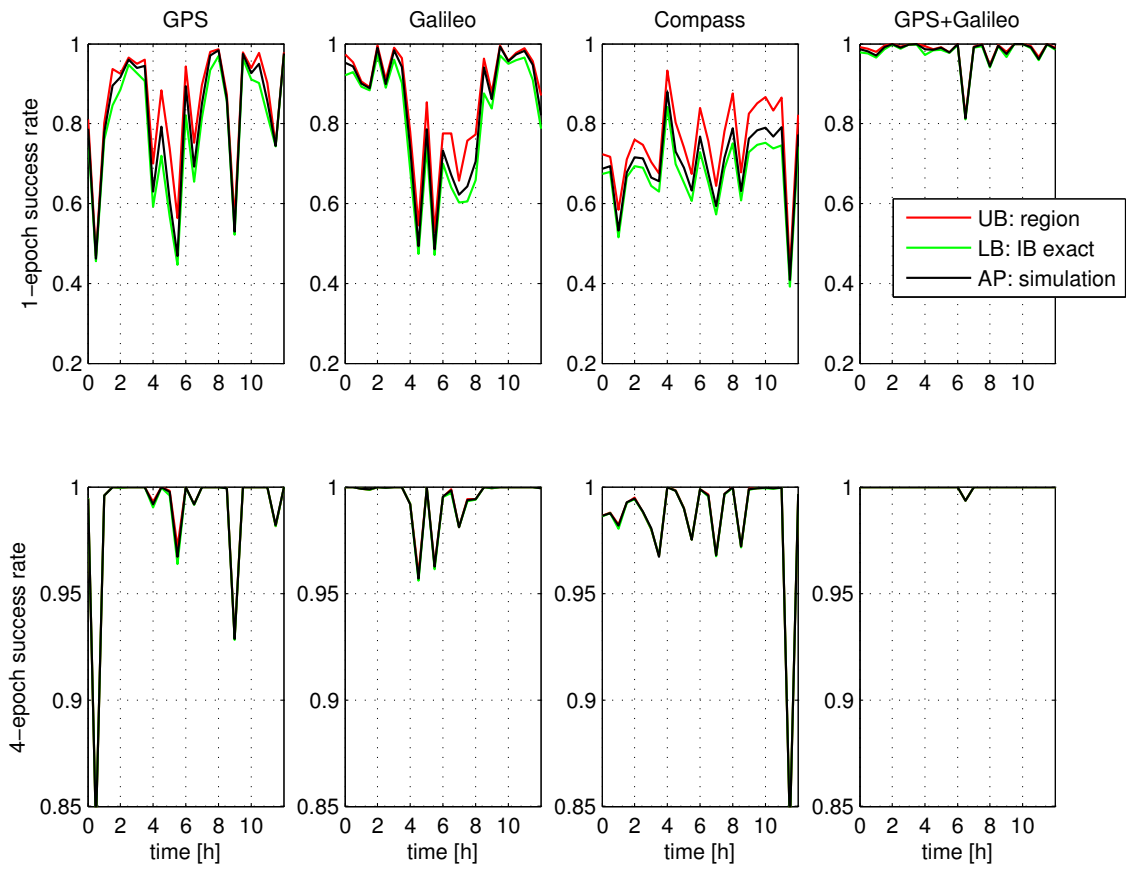


Figure 21: ILS success rates with GPS, Galileo, Compass or combined GPS+Galileo (from left to right) for a 35km baseline in Perth, Australia on 22-March-2012, 0:00 - 12:00 UTC. Top: 1-epoch model. Bottom: 4-epoch model.

720 *Further analysis*

721 The example shown here could easily be extended to study for example the
 722 benefit of having more Compass satellites available in the future, the effect of
 723 using different signals (i.e. frequencies), or the effect of different baseline lengths.

724 **7. Concluding remarks**

725 In this contribution the Matlab toolbox Ps-LAMBDA is presented, which al-
726 lows a user to compute different bounds and approximations of the success rate
727 of integer estimation. All bounds and approximations from Section 5 have been
728 included in the software since it was shown that it will depend very much on the
729 model at hand which bounds and approximations are sharpest. By default the tool
730 will calculate the exact IB success rate for the decorrelated ambiguities, since for
731 GNSS models this provides a sharp lower bound to the ILS success rate, and an
732 upper bound for the IR success rate.

733 We have focused here on GNSS models, but Ps-LAMBDA can be used for any
734 integer estimation problem; the only input required is the variance-covariance ma-
735 trix of the real-valued estimates of the integer parameters. As such, Ps-LAMBDA
736 is a valuable tool for many applications that rely on the precise phase observa-
737 tions from GNSS or other interferometric techniques. Firstly, Ps-LAMBDA can
738 be used for research and design purposes as to decide on which system and sig-
739 nals to use, to select the best time to take measurements, to know beforehand how
740 many epochs of data will be required to ensure reliable ambiguity resolution, or
741 to analyze whether successful ambiguity resolution for a given baseline length is
742 feasible. Secondly, the tool can be used for deciding on acceptance of the integer
743 ambiguity solution in real data processing.

744 In the presence of unmodeled biases, such as multipath, the probability of
745 correct integer estimation will be negatively affected. For studying the bias-
746 robustness or -sensitivity of ambiguity resolution, it will be useful to analyze the
747 impact of a given bias on the success rate. A future version of the Ps-LAMBDA
748 will therefore include an option to evaluate the bias-affected success rates as well.

749 The Ps-LAMBDA toolbox is available upon request from the authors.

750 **Acknowledgments**

751 This work has been executed in the framework of the Positioning Program
752 Project 1.01 New carrier phase processing strategies for achieving precise and re-
753 liable multi-satellite, multi-frequency GNSS/RNSS positioning in Australia of the
754 Cooperative Research Centre for Spatial Information, whose activities are funded
755 by the Australian Commonwealth's Cooperative Research Centres Programme.

756 Peter J.G. Teunissen is the recipient of an Australian Research Council (ARC)
757 Federation Fellowship (project number FF0883188). All this support is gratefully
758 acknowledged.

759 Bevis, M., Businger, S., Herring, T. A., Rocken, C., Anthes, R. A., Ware, R. H.,
760 1992. GPS meteorology: remote sensing of atmospheric water vapor using the
761 Global Positioning System. *Journal of Geophysical Research* 97, 15787–15801.

762 Blewitt, G., 1989. Carrier phase ambiguity resolution for the global positioning
763 system applied to geodetic baselines up to 2000 km. *Journal of Geophysical*
764 *Research* 94, 135 – 151.

765 Bock, Y., 1996. Medium distance GPS measurements. In: PJG Teunissen and A
766 Kleusberg, *GPS for Geodesy*, Springer-Verlag, Berlin.

767 Buist, P., Teunissen, P., Giorgi, G., Verhagen, S., 2010. Multivariate Bootstrapped
768 Relative Positioning of Spacecraft Using GPS L1/Galileo E1 Signals. *Advances*
769 *in Space Research* 47 (5), 770–785.

- 770 Chang, X., Yang, X., Zhou, T., 2005. MLAMBDA: a modified LAMBDA method
771 for integer least-squares estimation. *Journal of Geodesy* 79, 552–565.
- 772 Collins, P., Bisnath, S., Lahaye, F., Heroux, P., 2009. Undifferenced GPS ambi-
773 guity resolution using the decoupled clock model and ambiguity datum fixing.
774 *Navigation* 57 (2), 123–135.
- 775 Dai, Z., Knedlik, S., Loffeld, O., 2009. Instantaneous triple-frequency GPS cycle-
776 slip detection and repair. *International Journal of Navigation and Observation*
777 ID 407231, 1–15.
- 778 Das Neves Viegas, D. C., Cunha, S. R., 2007. Precise positioning by phase pro-
779 cessing of sound waves. *IEEE Trans. Signal Process.* 55 (12), 5731–5738.
- 780 De Jonge, P. J., Tiberius, C., 1996. The LAMBDA method for integer ambigu-
781 ity estimation: implementation aspects, LGR-Series, No 12. Tech. rep., Delft
782 University of Technology.
- 783 deLacy, M. C., Reguzzoni, M., Sansò, F., 2011. Real-time cycle slip detection in
784 triple-frequency GNSS. *GPS Solutions Online first*, 1–10.
- 785 Dong, D., Bock, Y., 1989. Global positioning system network analysis with phase
786 ambiguity resolution applied to crustal deformation studies in California. *Jour-
787 nal of Geophysical Research* 94 (B4), 3949–3966.
- 788 Euler, H. J., Seeger, S., Zelzer, O., Takac, F., Zebhauser, B. E., 2004. Improvement
789 of Positioning Performance Using Standardized Network RTK Messages. In:
790 *Proc. of ION NTM 2004, San Diego CA.* pp. 453–461.

- 791 Everaerts, J., 2008. The use of Unmanned Aerial Vehicles (UAVS) for remote
792 sensing and mapping. *The International Archives of the Photogrammetry, Re-*
793 *mote Sensing and Spatial Information Sciences XXXVII (B1)*, 1187–1192.
- 794 Fernandes, R. M. S., Ambrosius, B. A. C., Noomen, R., Bastos, L., Miranda,
795 L. C. M., Spakman, W., 2004. Angular velocities of Nubia and Somalia from
796 continuous GPS data: implications on present-day relative kinematics. *Earth*
797 *and Planetary Science Letters* 222, 197–208.
- 798 Geng, J., Shi, C., Ge, M., Dodson, A., Lou, Y., Zhao, Q., Liu, J., 2012. Improv-
799 ing the estimation of fractional-cycle biases for ambiguity resolution in precise
800 point positioning. *Journal of Geodesy* 86, 579–589.
801 URL <http://dx.doi.org/10.1007/s00190-011-0537-0>
- 802 Hanssen, R. F., Teunissen, P. J. G., Joosten, P., 2001. Phase ambiguity resolution
803 for stacked radar interferometric data. *Proc. of the International Symposium on*
804 *Kinematic Systems in Geodesy, GeomaticsandNavigation,Banff, Canada*, 317–
805 320.
- 806 Hassibi, A., Boyd, S., 1998. Integer parameter estimation in linear models with
807 applications to GPS. *IEEE Transactions on Signal Processing* 46 (11), 2938
808 –2952.
- 809 Heroux, P., Kouba, J., 1995. GPS precise point positioning with a difference. In:
810 *Geomatics 95, Ottawa, Ontario, Canada*.
- 811 Hobiger, T., Sekido, M., Koyama, Y., Kondo, T., 2009. Integer phase ambigu-
812 ity estimation in next-generation geodetic Very Long Baseline Interferometry.
813 *Advances in Space Research* 43, 187–192.

- 814 Hofmann-Wellenhof, B., Lichtenegger, H., Collins, J., 2001. Global positioning
815 system: theory and practice, 5th edn. Springer Berlin Heidelberg, New York.
- 816 Hofmann-Wellenhof, B., Lichtenegger, H., Wasle, E., 2008. GNSS global naviga-
817 tion systems: GPS, GLONASS, Galileo and More. Springer, Wien.
- 818 Huber, S., Younis, M., Krieger, G., 2010. The TanDEM-X mission: overview and
819 interferometric performance. *International Journal of Microwave and Wireless*
820 *Technologies* 2, 379–389.
- 821 Kondo, K., 2003. Optimal success/error rate and its calculation in resolution of
822 integer ambiguities in carrier phase positioning of Global Positioning System
823 (GPS) and Global Navigation Satellite System (GNSS). In: *Proc. of ION An-
824 nual Meeting, Albuquerque NM.* pp. 176–187.
- 825 Kroes, R., Montenbruck, O., Bertiger, W., Visser, P., 2005. Precise GRACE base-
826 line determination using GPS. *GPS Solutions* 9 (1), 21–31.
- 827 Laurichesse, D., Mercier, F., Berthias, J. P., Broca, P., Cerri, L., 2009. Integer am-
828 biguity resolution undifferenced GPS phase measurements and its application
829 to PPP and satellite precise orbit determination. *Navigation* 56 (2), 135–149.
- 830 Leick, A., 2004. *GPS satellite surveying.* 3rd edn. John Wiley, New York.
- 831 Leung, S., Montenbruck, O., 2005. Real-Time Navigation of formation flying
832 spacecraft using GPS measurements. *Journal of Guidance, Control, and Dy-
833 namics* 28 (2), 226–235.
- 834 Li, B., Teunissen, P. J. G., 2011. High dimensional integer ambiguity resolution:

- 835 A first comparison between LAMBDA and Bernese. *The Journal of Navigation*
836 64, S192–S210.
- 837 Michel, G. W., Yu, Y. Q., Zhu, S. Y., Reigber, C., Becker, M., Reinhart and WSi-
838 mons, E., Ambrosius, B., Vigny, C., Chamot-Rooke, N., Le Pichon and PMor-
839 gan, X., Matheussen, S., 2001. Crustal motion and block behaviour in SE-Asia
840 from GPS measurements. *Earth and Planetary Science Letters* 187, 239–244.
- 841 Misra, P., Enge, P., 2001. *Global Positioning System: Signals, Measurements, and*
842 *Performance*. Ganga-Jamuna Press, Lincoln MA.
- 843 Nadarajah, N., Teunissen, P. J. G., Buist, P. J., 2012. Attitude determination of
844 LEO satellites using an array of GNSS sensors. Accepted for publication in
845 *Proc. of IEEE Fusion*.
- 846 Odijk, D., 2002. Fast precise GPS positioning in the presence of ionospheric de-
847 lays. Ph.D. thesis, *Publications on Geodesy*, 52, Netherlands Geodetic Com-
848 mission, Delft.
- 849 Odijk, D., Teunissen, P. J. G., 2008. ADOP in closed form for a hierarchy of multi-
850 frequency single-baseline GNSS models. *Journal of Geodesy* 82, 473–492.
- 851 Odijk, D., Teunissen, P. J. G., Zhang, B., 2012. Single-frequency integer ambi-
852 guity resolution enabled precise point positioning. *Journal of Surveying Engi-
853 neering* 2012, DOI:10.1061/(ASCE)SU.1943–5428.0000085.
- 854 Rieke, M., Foerster, T., Geipel, J., Prinz, T., 2011. High-precision position-
855 ing and real-time data processing of UAV-systems. *The International Archives*
856 *of the Photogrammetry, Remote Sensing and Spatial Information Sciences*
857 XXXVIII (1-C22), 1–6.

- 858 Schon, S., Brunner, F. K., 2008. Atmospheric turbulence theory applied to GPS
859 carrier-phase data. *Journal of Geodesy* 82, 47–57.
- 860 Strang, G., Borre, K., 1997. *Linear Algebra, Geodesy, and GPS*. Wellesley-
861 Cambridge Press, Wellesley MA.
- 862 Takac, F., Zelzer, O., 2008. The Relationship Between Network RTK Solutions
863 MAC, VRS, PRS, FKP and i-MAX. In: *Proc. of ION GNSS 2008*, Savannah
864 GA. pp. 348–355.
- 865 Teunissen, P. J. G., 1993. Least squares estimation of the integer GPS ambiguities.
866 In: *Invited lecture, Section IV Theory and Methodology, IAG General Meeting*,
867 Beijing.
- 868 Teunissen, P. J. G., 1994. A new method for fast carrier phase ambiguity esti-
869 mation. In: *Proceedings IEEE Position, Location and Navigation Symposium*
870 *PLANS'94*. Las Vegas, NV, pp. 562–573.
- 871 Teunissen, P. J. G., 1995a. The invertible GPS ambiguity transformations.
872 *Manuscripta Geodaetica* 20, 489–497.
- 873 Teunissen, P. J. G., 1995b. The least-squares ambiguity decorrelation adjustment:
874 a method for fast GPS integer ambiguity estimation. *Journal of Geodesy* 70,
875 65–82.
- 876 Teunissen, P. J. G., 1997. A canonical theory for short GPS baselines. Part IV:
877 Precision versus reliability. *Journal of Geodesy* 71, 513–525.
- 878 Teunissen, P. J. G., 1998a. On the integer normal distribution of the GPS ambigu-
879 ities. *Artificial Satellites* 33 (2), 49–64.

- 880 Teunissen, P. J. G., 1998b. Success probability of integer GPS ambiguity rounding
881 and bootstrapping. *Journal of Geodesy* 72, 606–612.
- 882 Teunissen, P. J. G., 1999a. An optimality property of the integer least-squares
883 estimator. *Journal of Geodesy* 73 (11), 587–593.
- 884 Teunissen, P. J. G., 1999b. The probability distribution of the GPS baseline for a
885 class of integer ambiguity estimators. *Journal of Geodesy* 73, 275 –284.
- 886 Teunissen, P. J. G., 2000. ADOP based upperbounds for the bootstrapped and the
887 least-squares ambiguity success rates. *Artificial Satellites* 35 (4), 171–179.
- 888 Teunissen, P. J. G., Kleusberg, A., 1998. *GPS for geodesy*, 2nd edn. Springer
889 Berlin Heidelberg New York.
- 890 Teunissen, P. J. G., Odijk, D., 1997. Ambiguity Dilution of Precision: definition,
891 properties and application. In: *Proc. of ION GPS-1997*, Kansas City MO. pp.
892 891–899.
- 893 Thomsen, H. F., 2000. Evaluation of upper and lower bounds on the success prob-
894 ability. *Proc. of ION GPS-2000*, Salt Lake City UT, 183–188.
- 895 Todorova, S., Hobiger, T., Schuh, H., 2008. Using the Global Navigation Satellite
896 System and satellite altimetry for combined Global Ionosphere Maps. *Advances*
897 *in Space Research*, 727–736.
- 898 Van der Hoeven, A., Hanssen, R. F., Ambrosius, B., 2002. Tropospheric delay esti-
899 mation and analysis using GPS and SAR interferometry. *Physics and Chemistry*
900 *of the Earth* 27, 385–390.

- 901 Verhagen, S., 2005. On the reliability of integer ambiguity resolution. *Navigation*
902 52 (2), 99–110.
- 903 Wickert, J., Schmidt, T., Michalak, G., Heise, S., Arras, C., Falck, G. B. C., König,
904 R., Pingel, D., Rothacher, M., 2009. GPS Radio Occultation with CHAMP,
905 GRACE-A, SAC-C, TerraSAR-X, and FORMOSAT-3/COSMIC: Brief Review
906 of Results from GFZ. In: *New Horizons in Occultation Research*. A. K. Steiner,
907 B. Pirscher, U. Foelsche, G. Kirchengast (Eds.). Springer-Verlag, Berlin, pp. 3–
908 15.
- 909 Wu, Y., Jin, S. G., Wang, Z. M., Liu, J. B., 2010. Cycle-slip detection using
910 multi-frequency GPS carrier phase observations: a simulation study. *Advances*
911 *in Space Research* 46, 144–149.
- 912 Zumberge, J. F., Heflin, M. B., Jefferson, D. C., Watkins, M. M., Webb, F. H.,
913 1997. Precise point positioning for the efficient and robust analysis of GPS data
914 from large networks. *Journal of Geophysical Research* 102, 5005–5017.

List of Figures

1	Position errors in East (dE), North (dN) and Up (dU) direction in meters for ambiguity float solutions (top panel), ambiguity fixed solutions (bottom panel). Note the different scales in the top and bottom panels.	10
2	Scatterplot of horizontal position errors in meters for float solution (grey dots) and corresponding fixed solution. In this case, 93% of the solutions were correctly fixed (green dots), and 7% was wrongly fixed (red dots).	12
3	2D Pull-in regions for integer rounding (IR) and 50,000 float solutions. Top: original ambiguities \hat{a} [cycles]; Bottom: \mathbf{Z} -decorrelated ambiguities \hat{z} [cycles].	15
4	2D pull-in regions for integer bootstrapping (IB) and 50,000 float solutions. Top: original ambiguities \hat{a} [cycles]; Bottom: \mathbf{Z} -decorrelated ambiguities \hat{z} [cycles].	17
5	2D pull-in regions for integer least squares (ILS) and 50,000 float solutions. Top: original ambiguities \hat{a} [cycles]; Bottom: \mathbf{Z} -decorrelated ambiguities \hat{z} [cycles].	19
6	Top: PDF and 2D pull-in regions for ILS. Bottom: corresponding probability mass function.	22
7	Ps-LAMBDA: overview of available methods and options in routine SuccessRate. Default option is indicated with (*). Names of underlying routines are shown as well. AP = approximation (blue), LB = lower bound (green), UB = upper bound (red).	23
8	Examples of simulation-based success rate as function of number of samples. Each panel shows the results for a different GNSS model.	28
9	IR success rates: upper bound based on IB (red) and lower bound based on diagonal VC-matrix (green) versus the actual IR success rate for the models from Table 3.	31

10	IB success rates: ADOP-based upper bound versus the exact IB success rate for the models from Table 3.	31
11	ILS success rates: lower bound based on IB (green) and upper bound based on ADOP (red) versus the actual ILS success rate for the models from Table 3.	34
12	ILS success rates: ADOP-based approximation versus the actual ILS success rate for the models from Table 3.	34
13	Two examples of the ellipsoidal region (green) contained by the pull-in region $\mathcal{P}_{0,ILS}$ (different shape of pull-in regions is due to different VC-matrices $\mathbf{Q}_{\hat{z}\hat{z}}$).	36
14	Integration region (red) containing $\mathcal{P}_{0,ILS}$ and defined by the intersection of two banded subsets.	36
15	ILS success rates: lower and upper bounds based on bounding the integration region versus the actual ILS success rate for the models from Table 3.	38
16	ILS success rates: lower and upper bounds based on bounding the VC-matrix versus the actual ILS success rate for the models from Table 3.	39
17	ILS success rate bounds for 2-frequency geometry-free model with 2 ambiguities, f is the scale factor applied to the VC-matrix (bottom panel shows same results, but only for smaller f).	40
18	ILS success rate bounds based on bounding the (2×2) scaled VC-matrix with both variances equal to 0.02, and covariance equal to 0.0005. The scale factor is equal to f	42
19	Skyplots of GPS (left), Galileo (middle) and Compass (right) for Perth, Australia on 22-March-2012, 0:00 - 12:00 UTC. The plots show the azimuth [deg] and elevation [deg] of the satellites; the dots correspond to the satellite positions at 6:00 UTC.	44

20	Number of visible satellites in Perth, Australia on 22-March-2012, 0:00 - 12:00 UTC.	44
21	ILS success rates with GPS, Galileo, Compass or combined GPS+Galileo (from left to right) for a 35km baseline in Perth, Australia on 22-March-2012, 0:00 - 12:00 UTC. Top: 1-epoch model. Bottom: 4-epoch model. . .	47

List of Tables

1	Overview of GNSS frequencies of open signals.	6
2	Percentage of float solutions that is correctly fixed for the three integer estimation methods (corresponding to Figures 3 to 5).	20
3	Measurement scenarios used in Section 5 (standard deviations apply to zenith direction).	27